Decomposing Imaginary-Time Feynman Diagrams Using Separable Basis Functions: Anderson Impurity Model Strong-Coupling Expansion

Jason Kaye,[1,2,*] Zhen Huang,[3,1] Hugo U. R. Strand,[4,5] and Denis Golež[6,7]

[1]*Center for Computational Quantum Physics, Flatiron Institute, 162 5th Avenue, New York, New York 10010, USA*
[2]*Center for Computational Mathematics, Flatiron Institute, 162 5th Avenue, New York, New York 10010, USA*
[3]*Department of Mathematics, University of California, Berkeley, California 94720, USA*
[4]*School of Science and Technology, Örebro University, SE-701 82 Örebro, Sweden*
[5]*Institute for Molecules and Materials, Radboud University, 6525 AJ Nijmegen, The Netherlands*
[6]*Jožef Stefan Institute, Jamova 39, SI-1000, Ljubljana, Slovenia*
[7]*Faculty of Mathematics and Physics, University of Ljubljana, Jadranska 19, 1000 Ljubljana, Slovenia*

(Received 20 July 2023; revised 15 April 2024; accepted 20 May 2024; published 26 August 2024; corrected 2 May 2025)

We present a deterministic algorithm for the efficient evaluation of imaginary-time diagrams based on the recently introduced discrete Lehmann representation (DLR) of imaginary-time Green's functions. In addition to the efficient discretization of diagrammatic integrals afforded by its approximation properties, the DLR basis is separable in imaginary-time, allowing us to decompose diagrams into linear combinations of nested sequences of one-dimensional products and convolutions. Focusing on the strong-coupling bold-line expansion of generalized Anderson impurity models, we show that our strategy reduces the computational complexity of evaluating an Mth-order diagram at inverse temperature β and spectral width $\omega_{\max}$ from $\mathcal{O}((\beta\omega_{\max})^{2M-1})$ for a direct quadrature to $\mathcal{O}(M(\log(\beta\omega_{\max}))^{M+1})$, with controllable high-order accuracy. We benchmark our algorithm using third-order expansions for multiband impurity problems with off-diagonal hybridization and spin-orbit coupling, presenting comparisons with exact diagonalization and quantum Monte Carlo approaches. In particular, we perform a self-consistent dynamical mean-field theory calculation for a three-band Hubbard model with strong spin-orbit coupling representing a minimal model of Ca_2RuO_4, demonstrating the promise of the method for modeling realistic strongly correlated multiband materials. For both strong and weak coupling expansions of low and intermediate order, in which diagrams can be enumerated, our method provides an efficient, straightforward, and robust blackbox evaluation procedure. In this sense, it fills a gap between diagrammatic approximations of the lowest order, which are simple and inexpensive but inaccurate, and those based on Monte Carlo sampling of high-order diagrams.

DOI: 10.1103/PhysRevX.14.031034

Subject Areas: Computational Physics, Condensed Matter Physics, Strongly Correlated Materials

I. INTRODUCTION

Feynman diagram expansions are a standard computational tool in quantum many-body physics, both in condensed matter and quantum chemistry [1–4]. Given a Hamiltonian, one expands around an exactly solvable limit, such as the noninteracting (or atomic) limit, and interaction (or atom-atom coupling) corrections are captured by summing diagrams up to some order. Directly evaluated low-order expansions, like Hartree-Fock and Hedin's GW method [5], are routinely used in chemistry and solid-state physics first-principles calculations [4,6,7]. Similarly, the first-order bold expansion about the atomic limit, also called the noncrossing approximation (NCA), is widely used for quantum impurity problems [8–13]. While such low-order expansions are simple, inexpensive, and reliable for systems close to the exactly solvable limit, they are inadequate in the nonperturbative regime. In certain cases, such as the description of Kondo resonances in impurity problems, including diagrams of even slightly higher order is required for the correct recovery of physical observables [13–16]. However, direct evaluation of high-order expansions requires high-dimensional quadrature, rendering it impractical beyond even the first few orders.

*Contact author: jkaye@flatironinstitute.org

We illustrate the state of the field for the example of the bold hybridization expansions of the Anderson impurity model, which we focus on in this work. Here, the first-order NCA, which requires no integration, is used routinely [1,12,17–19], as is the second-order one-crossing approximation (OCA), which requires only two-dimensional integration [12,14,20–24]. At third order and beyond, we are aware of only a few studies because of the rapidly growing cost of direct quadrature [12,16,25], though expansions at this order describe the physics around the Mott transition remarkably well. A notable recent exception involves a combination of a three-point vertex computed by direct quadrature and Monte Carlo sampling of the four-point vertex [26,27]. Thus, although direct evaluation methods are simple, robust, and can be made high-order accurate with respect to quadrature error (see Sec. III C), they have thus far been almost entirely restricted to the lowest-order diagrammatic expansions, limiting their usefulness in addressing challenging, material-realistic models.

In the opposite regime of very high-order expansions, diagrammatic Monte Carlo methods for sampling over diagram orders, topologies, and integrals have led to enormous success in producing accurate results for sophisticated, strongly correlated systems, including quantum impurity problems [2,28–31] in combination with dynamical mean-field theory (DMFT) [1,32], polaron problems [33–35], and lattice Hubbard problems [36–39]. However, such approaches are computationally intensive, slowly converging (at the half-order Monte Carlo or first-order quasi-Monte Carlo [40,41] rate), and, in many cases, lack robustness due to the sign problem [2]. In DMFT applications, the sign problem has prevented the application of Monte Carlo-based methods to a large class of materials, such as multiband systems with off-diagonal hybridization [42], e.g., spin-orbit coupled 4d and 5d electron systems. For several prominent correlated materials, the sign problem has been mitigated by employing a basis transformation within the interaction expansion [43,44], but this approach is limited to rather high temperatures. Another approach, the inchworm Monte Carlo formulation of the strong-coupling expansion [42,45], has been shown to mitigate the sign problem in minimal impurity models, and its range of applicability is being actively explored. A promising recent development, the tensor train diagrammatics method, uses tensor cross interpolation (TCI) rather than Monte Carlo sampling, and it was used to compute high-order bare expansions of the Anderson impurity problem, both for the interaction [46] and hybridization [47] expansions, without a sign problem and with convergence rates significantly faster than Monte Carlo methods. This technique is related in several ways to the algorithm presented here; however, at present, it has been used primarily for high-order bare expansion diagrams, and since it relies on a specific underlying compressibility structure of the integrand, its range of applicability is not yet well understood.

An opportunity therefore exists for the development of diagram evaluation techniques which maintain the simplicity and robustness of direct methods at the lowest orders while extending their range of applicability at least to intermediate orders. Indeed, practitioners typically switch to diagrammatic Monte Carlo methods even when the required expansion order is only slightly beyond the reach of direct methods, due to the lack of practical alternatives [15,27]. By exploiting the specific structure of imaginary-time diagrams, we obtain a method which aims to make such calculations routine, deterministic, and high-order accurate. It relies on the recently introduced discrete Lehmann representation (DLR), which provides a compact basis of exponentials in which to expand arbitrary single-particle imaginary-time Green's functions, and related quantities, with high-order accuracy [48]. Beyond the favorable discretization properties of the DLR, we show that the separability of the DLR basis functions in their imaginary-time argument can be used to decompose diagrams into linear combinations of nested sequences of products and convolutions. These products and convolutions are then computed efficiently in the DLR basis. Whereas the cost of direct evaluation of an Mth-order diagram scales with the inverse temperature β and spectral width $\omega_{\max}$ as $\mathcal{O}((\beta\omega_{\max})^{2M-1})$, our proposed method scales as $\mathcal{O}(M(\log(\beta\omega_{\max}))^{M+1})$. The method is trivially parallelizable over the large number of diagrams appearing in typical diagrammatic calculations.

We implement our algorithm for the strong-coupling expansion up to third order and benchmark it on several challenging Anderson impurity problems. We observe rapid order-by-order convergence within the Mott insulating regime for systems with off-diagonal hybridization and/or strong local spin-orbit coupling. We also solve a minimal model for the strongly correlated calcium ruthenate Ca_2RuO_4 within DMFT [49–53]. The significant spin-orbit coupling in this material makes it a challenging problem for Monte Carlo-based methods [43], but we show that the third-order solution is highly accurate. A general implementation of our approach beyond third-order diagrams and to weak coupling expansions is straightforward, requiring only technical effort, and our formalism indicates a clear path towards extension to systems beyond impurity problems, like molecular or extended systems. The main idea of our algorithm—separation of variables using sum-of-exponentials approximations—may be applicable to higher-order quantum many-body expansions comprising higher-dimensional correlators and kernels, such as the triangular vertex functions in the Hedin equations [5,26,27,54] and the two-particle objects appearing in the Bethe-Salpeter equation [1,55]. Furthermore, our approach is likely complementary to other methods, such as TCI, which aim to address the exponential-scaling bottleneck of high-order diagrammatic calculations, providing a new ingredient in the design of algorithms based on these tools. This work therefore

represents a promising proof of concept, demonstrated on several challenging calculations, for a fundamental new tool in diagrammatic calculations.

II. OVERVIEW OF THE METHOD

The main idea of our algorithm can be demonstrated with a simple example whose structure is typical of imaginary-time Feynman diagrams. Consider the integral

$$I(\tau) = \int_0^\tau d\tau' \int_0^{\tau'} d\tau'' G_1(\tau-\tau'')G_2(\tau-\tau')G_3(\tau'-\tau''),$$

for scalar or matrix-valued G_i and $\tau \in [0,\beta]$. Since the factor G_1 couples the τ and τ'' variables, $I(\tau)$ must be calculated as a double integral. However, if we can make a low-rank approximation

$$G_1(\tau-\tau'') \approx \sum_{l=1}^{r} G_{1l}\varphi_l(\tau)\psi_l(\tau'') \tag{1}$$

with r small, for some scalar-valued φ_l and ψ_l, then we can separate variables:

$$I(\tau) \approx \sum_{l=1}^{r} G_{1l}\varphi_l(\tau) \int_0^\tau d\tau' G_2(\tau-\tau') \times \int_0^{\tau'} d\tau'' G_3(\tau'-\tau'')\psi_l(\tau'').$$

Then, $I(\tau)$ can be computed from r sequences of products and nested convolutions, which may be less expensive than computing a full double integral for each τ, particularly if the G_i and the product and convolution operations can be discretized efficiently. In the case of imaginary-time quantities, the DLR basis [48] provides an efficient discretization with the separability property (1). The number of basis functions scales as $r = \mathcal{O}(\log(\beta\omega_{\max})\log(1/\varepsilon))$, with ε a user-specified accuracy, for any G_1. We apply this separation-of-variables approach to certain hybridization functions appearing in the strong-coupling expansion and compute the resulting products and convolutions in the DLR basis. We also demonstrate its application to the weak coupling expansion in Appendix C.

Remark 1. In the applied and computational mathematics literature, separability in sum-of-exponentials approximations has been used to obtain fast algorithms for applying nonlocal integral operators in a variety of settings [56–59], including fast history integration and compression in Volterra integral equations [60–62] and nonlocal transparent boundary conditions [63–65], diagonal translation operators in the fast multipole method [66–68], the fast Gauss transform [69], the periodic fast multipole method [70], and others [71,72]. In these applications, one typically considers an integral transform $I(x) = \int dx' K(x-x')f(x')$ for a kernel K, which is known *a priori*, and uses a sum-of-exponentials approximation of K to separate "source" (internal or integration) variables x' from "target" (external) variables x. By contrast, Feynman diagrams involve higher-dimensional integrals connecting *a priori* unknown functions entangled via many internal and external variables.

III. BACKGROUND: DIAGRAMMATIC METHODS AND NUMERICAL TOOLS

A. Strong-coupling hybridization expansion

Quantum impurity problems are zero-dimensional interacting quantum many-body systems in contact with a general bath environment. The local part of the impurity Hamiltonian H_{loc} can have arbitrary quadratic terms $\epsilon_{\kappa\lambda}$ and quartic terms $U_{\kappa\lambda\mu\nu}$:

$$H_{\text{loc}} = \sum_{\kappa,\lambda=1}^{n} \epsilon_{\kappa\lambda} c_\kappa^\dagger c_\lambda + \sum_{\kappa,\lambda,\mu,\nu=1}^{n} U_{\kappa\lambda\mu\nu} c_\kappa^\dagger c_\lambda^\dagger c_\mu c_\nu. \tag{2}$$

Here, $c_\lambda^\dagger$ is the creation operator for a fermion in the impurity state λ and n is the number of impurity states. The full quantum impurity problem, including the coupling to the bath, can be described in terms of the action

$$\mathcal{S} = \int_0^\beta d\tau H_{\text{loc}}[c,c^\dagger] + \sum_{\kappa,\lambda=1}^{n} \int_0^\beta d\tau \int_0^\beta d\tau' c_\lambda^\dagger(\tau)\Delta_{\lambda\kappa}(\tau-\tau')c_\kappa(\tau'). \tag{3}$$

The hybridization function $\Delta_{\lambda\kappa}(\tau-\tau')$ describes the propagation of a fermion in impurity state κ entering the bath at time τ' and returning to the impurity state λ at time τ. Note that $\Delta_{\lambda\kappa}$ is a scalar-valued function for each fixed κ and λ.

The properties of the impurity problem can be characterized in terms of static expectation values and dynamical response functions. We focus here on the single-particle Green's function $G_{\lambda\kappa}(\tau-\tau') = -\langle \mathcal{T} c_\lambda(\tau) c_\kappa^\dagger(\tau')\rangle$, which describes the temporal correlation between the addition of a fermion to the impurity in state κ and the removal of a fermion in state λ. In the noninteracting limit $U_{\kappa\lambda\mu\nu} = 0$, the Green's function can be determined analytically, and for nonzero interactions, one can carry out an expansion in the interaction parameter, called the interaction expansion. However, for many strongly correlated systems, this becomes infeasible, requiring high expansion orders [73,74]. For sufficiently strong interactions, the series diverges with perturbation order, requiring tailored resummations derived from conformal transformations [75].

In the limit of an impurity decoupled from the bath (zero hybridization $\Delta_{\lambda\kappa} = 0$), we can directly diagonalize H_{loc} since there are a finite number of local many-body states. This is the starting point of the strong-coupling expansion, which is, in essence, a perturbative expansion in the hybridization function. We refer to Ref. [12] for a detailed

description of this approach and briefly summarize its main characteristics here.

To enable the hybridization expansion, the impurity action $\mathcal{S}$ is rewritten by introducing a pseudoparticle $p_k^\dagger|0\rangle$ for each impurity many-body state $|k\rangle$, making the local Hamiltonian quadratic and the hybridization quartic in the pseudoparticle space. The resulting action is given by

$$\begin{aligned}\mathcal{S} = &\sum_{j,k=1}^{N}\int_0^\beta d\tau p_j^\dagger(\tau)\langle j|H_{\mathrm{loc}}|k\rangle p_k(\tau)\\ &+\sum_{j,k,j',k'=1}^{N}\sum_{\kappa,\lambda=1}^{n}\int_0^\beta d\tau\int_0^\beta d\tau' p_j^\dagger(\tau)p_k(\tau)F_{\lambda jk}^\dagger\\ &\times\Delta_{\lambda\kappa}(\tau-\tau')F_{\kappa k'j'}p_{k'}^\dagger(\tau')p_{j'}(\tau'),\end{aligned}\tag{4}$$

where $N=2^n$ is the number of local many-body states and $F_{\kappa jk}=\langle j|c_\kappa|k\rangle$. This action can be expanded in the quartic hybridization term. The pseudoparticle Green's function $\mathcal{G}_{jk}(\tau-\tau')=-\langle\mathcal{T}p_j(\tau)p_k^\dagger(\tau')\rangle$ satisfies the Dyson equation

$$\mathcal{G}=g+g*\Sigma*\mathcal{G},\tag{5}$$

where Σ is the pseudoparticle self-energy, $g_{jk}(\tau-\tau')=-\langle\mathcal{T}p_j(\tau)p_k^\dagger(\tau')\rangle_{\Delta=0}$ is the noninteracting ($\Delta=0$) pseudoparticle Green's function, and $*$ denotes the time-ordered convolution

$$(a*b)_{jk}(\tau)=\sum_{l=1}^{N}\int_0^\tau d\tau' a_{jl}(\tau-\tau')b_{lk}(\tau').$$

The pseudoparticle self-energy Σ contains the following sequence of diagrams:

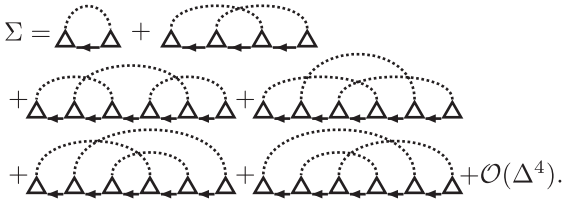

(6)

Solid lines correspond to the pseudoparticle Green's function:

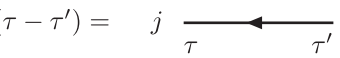

Each undirected dotted line,

(7)

corresponds to a sum over forward and backward propagation of the hybridization function interaction. A forward hybridization function interaction is represented by

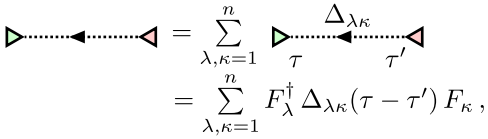

(8)

which, in turn, contains a sum over hybridization functions $\Delta_{\lambda\kappa}$. Here, F_κ, represented by a red triangle, is an $N\times N$ matrix with entries $F_{\kappa mn}$, and similarly for $F_\lambda^\dagger$, which is represented by a green triangle [see Eqs. (7) and (8)]. A backward interaction is given by

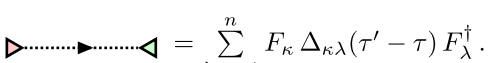

(9)

The order M of each self-energy diagram in Eq. (6) is given by the number of hybridization interactions (dotted lines) propagating either forward or backward. Each diagram is composed of a backbone of forward-propagating pseudoparticle Green's functions $\mathcal{G}$ (solid lines) connected by vertices associated with one end of a hybridization line. Each vertex represents an insertion of a matrix $F_\lambda^\dagger$ or F_κ at a given time τ_i. The internal times $\tau_1,\ldots,\tau_{2M-2}$ are integrated over in the domain $\tau_1\le\cdots\le\tau_{2M-2}\le\tau$. The prefactor of each diagram is $(-1)^{s+f+M}$, where s is the number of crossing hybridization lines and f is the number of backward-propagating hybridization lines. We give specific examples with mathematical expressions in the next subsection.

The single-particle Green's function $G(\tau)$ can be recovered from the pseudoparticle Green's function $\mathcal{G}$ using the circular diagram series

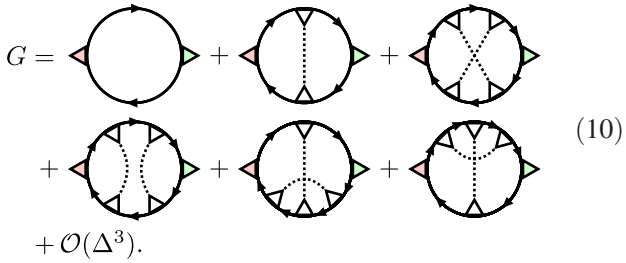

(10)

We again describe the construction of these diagrams and give examples in the next subsection. In this case, the diagram order M is one more than the number of hybridization interactions (dotted lines). Each diagram consists of a closed loop of pseudoparticle propagators $\mathcal{G}$ with two extra operator vertices F_λ and $F_\kappa^\dagger$ inserted at the times τ and 0 (red and green triangles, respectively). Here, λ and κ are the single-particle state indices of the single-particle Green's function $G_{\lambda\kappa}(\tau-0)$. The hybridization interactions and associated vertices have the same structure as in the self-energy diagrams. For $M>1$, the internal times $\tau_1,\ldots,\tau_{2M-2}$ are integrated over in the domain $0\le\tau_1\le\cdots\le\tau\le\cdots\le\tau_{2M-2}\le\beta$. The number

of internal times on the intervals $[0,\tau]$ and $[\tau,\beta]$, respectively, varies from one diagram to another. A trace is taken over the N-dimensional pseudoparticle state indices. The sign of a diagram is determined by first inserting a hybridization line between the two external times τ and 0 and then cutting an arbitrary pseudoparticle propagator. The prefactor is obtained from the modified diagram as $(-1)^{s+f+M}$.

The steps required to compute the single-particle Green's function G can be summarized as follows: (i) The pseudoparticle Green's function $\mathcal{G}$ and self-energy Σ are determined self-consistently by solving the Dyson equation (5), using the self-energy expansion (6); (ii) G is then obtained by evaluating the diagrams in Eq. (10).

B. Examples of diagrams

Both the self-energy diagrams and the circular diagrams for the single-particle Green's function beyond first order take the form of multidimensional integrals in imaginary-time. We present typical examples for each case to elucidate their common structure.

1. Pseudoparticle self-energy diagrams

The approximation of the pseudoparticle self-energy that includes only first-order diagrams, called the NCA, requires multiplication of $N \times N$ matrices but no integration:

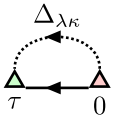

$$= (-1)^{0+0+1}\Delta_{\lambda\kappa}(\tau-0)F^{\dagger}_{\lambda}\,\mathcal{G}(\tau-0)\,F_{\kappa}. \tag{11}$$

The complete first-order contribution to Eq. (6) is given by

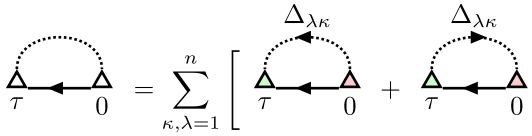

$$= \sum_{\kappa,\lambda=1}^{n} \left[\quad + \quad \right], \tag{12}$$

i.e., the sum over all hybridization directions [see Eq. (7)] and hybridization insertions $\Delta_{\lambda\kappa}$ [see Eqs. (8) and (9)].

The second-order approximation to the self-energy is called the one-crossing approximation (OCA), and contributing diagrams are given by double integrals:

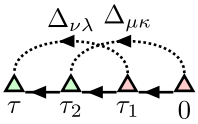

$$\begin{aligned} &= (-1)^{1+0+2} \\ &\times \int_0^{\tau} d\tau_2 \int_0^{\tau_2} d\tau_1\, \Delta_{\nu\lambda}(\tau-\tau_1)\Delta_{\mu\kappa}(\tau_2) \\ &\times F^{\dagger}_{\nu}\,\mathcal{G}(\tau-\tau_2)\,F^{\dagger}_{\mu}\,\mathcal{G}(\tau_2-\tau_1)\,F_{\lambda}\,\mathcal{G}(\tau_1)\,F_{\kappa}. \end{aligned} \tag{13}$$

The complete second-order contribution to Eq. (6) is obtained in a manner analogous to Eq. (12). We note that the factors corresponding to the forward-propagating backbone of impurity propagators have a repeated convolutional structure in the imaginary-time variables. This structure is broken by the hybridization functions, which couple nonadjacent time variables. All higher-order self-energy diagrams share this pattern. For example, the diagrams comprising the first third-order contribution in Eq. (6) are given by

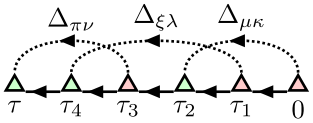

$$\begin{aligned} &= (-1)^{2+0+3} \int_0^{\tau} d\tau_4 \int_0^{\tau_4} d\tau_3 \int_0^{\tau_3} d\tau_2 \int_0^{\tau_2} d\tau_1\, \Delta_{\pi\nu}(\tau-\tau_3)\Delta_{\xi\lambda}(\tau_4-\tau_1)\Delta_{\mu\kappa}(\tau_2) \\ &\times F^{\dagger}_{\pi}\,\mathcal{G}(\tau-\tau_4)\,F^{\dagger}_{\xi}\,\mathcal{G}(\tau_4-\tau_3)\,F_{\nu}\,\mathcal{G}(\tau_3-\tau_2)\,F^{\dagger}_{\mu}\,\mathcal{G}(\tau_2-\tau_1)\,F_{\lambda}\,\mathcal{G}(\tau_1-0)\,F_{\kappa}. \end{aligned} \tag{14}$$

Our strategy will be to reinstate the convolutional structure of the backbone by separating variables in the hybridization functions.

2. Single-particle Green's function diagrams

The diagrams for the single-particle Green's function $G_{\lambda\kappa}(\tau) = -\langle \mathcal{T} c_{\lambda}(\tau) c^{\dagger}_{\kappa}(0)\rangle$ contain two additional operators compared with the self-energy diagrams: c_{λ} is inserted at time τ, and $c^{\dagger}_{\kappa}$ is inserted at time 0. The first-order (NCA) diagrams in Eq. (10) take the simple form

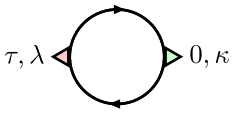

$$= (-1)^{0+0+0}\mathrm{Tr}\left[\mathcal{G}(\beta-\tau)\,F_{\lambda}\,\mathcal{G}(\tau)\,F^{\dagger}_{\kappa}\right]. \tag{15}$$

Since no hybridization function connects the times 0 and τ in these diagrams, the indices κ and λ are included in the notation. The second-order (OCA) diagrams contain a single hybridization insertion and two internal time integrals:

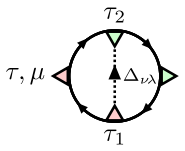

$$= (-1)^{1+0+1} \int_\tau^\beta d\tau_2 \int_0^\tau d\tau_1 \, \Delta_{\nu\lambda}(\tau_2 - \tau_1) \times \mathrm{Tr}\left[\mathcal{G}(\beta - \tau_2)\, F_\nu^\dagger\, \mathcal{G}(\tau_2 - \tau)\, F_\mu \times \mathcal{G}(\tau - \tau_1)\, F_\lambda\, \mathcal{G}(\tau_1)\, F_\kappa^\dagger\right]. \tag{16}$$

The third-order diagrams contain two hybridization insertions and four internal time integrals, e.g.,

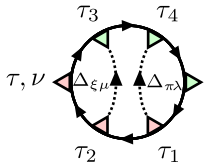

$$= (-1)^{2+0+2} \int_\tau^\beta d\tau_4 \int_\tau^{\tau_4} d\tau_3 \int_0^\tau d\tau_2 \int_0^{\tau_2} d\tau_1 \, \Delta_{\pi\lambda}(\tau_4 - \tau_1) \Delta_{\xi\mu}(\tau_3 - \tau_2) \tag{17}$$

$$\times \mathrm{Tr}\left[\mathcal{G}(\beta - \tau_4)\, F_\pi^\dagger\, \mathcal{G}(\tau_4 - \tau_3)\, F_\xi^\dagger\, \mathcal{G}(\tau_3 - \tau)\, F_\nu\, \mathcal{G}(\tau - \tau_2)\, F_\mu\, \mathcal{G}(\tau_2 - \tau_1)\, F_\lambda\, \mathcal{G}(\tau_1 - 0)\, F_\kappa^\dagger\right].$$

The backbone propagators again have a simple convolutional structure, now split into the two separable intervals $[0, \tau]$ and $[\tau, \beta]$, but the hybridization insertions again break this structure.

C. Evaluation by direct quadrature

In order to establish a baseline for comparison with our approach, we describe a simple integration strategy, based on equispaced quadrature rules, which has been employed in the literature [12,25,76]. Since we focus on the evaluation of individual diagrams, for the remaining discussion, we simplify notation by fixing the hybridization indices and absorbing the matrices F, $F^\dagger$ into the Green's functions. For example, we can write each OCA self-energy diagram (13) in the common form

$$\Sigma(\tau) = \int_0^\tau d\tau_2 \int_0^{\tau_2} d\tau_1 \Delta_2(\tau - \tau_1)\Delta_1(\tau_2) \times \mathcal{G}_3(\tau - \tau_2)\mathcal{G}_2(\tau_2 - \tau_1)\mathcal{G}_1(\tau_1), \tag{18}$$

where Σ and $\mathcal{G}_i$ are $N \times N$ matrix-valued and Δ_i are scalar valued.

A simple approach is to preevaluate all functions on an equispaced grid τ_j in imaginary-time and discretize the integrals by the second-order accurate trapezoidal rule. This approach reduces the double integral to

$$\Sigma(\tau_j) \approx \sum_{k_2=0}^{j}{}' \sum_{k_1=0}^{k_2}{}' \Delta_{2,j-k_1} \Delta_{1,k_2} \mathcal{G}_{3,j-k_2} \mathcal{G}_{2,k_2-k_1} \mathcal{G}_{1,k_1},$$

where we have used the notation $\Delta_{i,j} = \Delta_i(\tau_j)$. The prime on the sum indicates that its first and last terms are multiplied by the trapezoidal rule weight $1/2$, unless the sum contains only one term, in which case it is set to zero.

If n_τ grid points are used in each dimension, then this method scales as $\mathcal{O}(n_\tau^{2M-1})$ ($2M - 2$ internal time variables are integrated over for each τ). Furthermore, achieving convergence, in general, requires taking $n_\tau = \mathcal{O}(\beta\omega_{\max})$, with $\omega_{\max}$ the maximum spectral width of all quantities appearing in the integrand [48]. Defining the dimensionless constant $\Lambda = \beta\omega_{\max}$, the scaling of this method is $\mathcal{O}(\Lambda^{2M-1})$.

Remark 2. Although it does not improve the scaling with respect to M or Λ, the order of accuracy p—that is, the error convergence rate n_τ^{-p}, given by $p = 2$ for the trapezoidal rule—can be substantially improved at negligible additional cost using endpoint-corrected equispaced quadratures. For example, Gregory quadratures (yielding roughly $p \leq 10$), and more stable variants (yielding larger p) [77,78], increase the order of accuracy by reweighting a few endpoint values. For stability at very high-order accuracy, endpoint node locations must be modified, as in Alpert quadrature [79], requiring high-order accurate on-the-fly evaluation of the integrand for a small subset of terms. To our knowledge, such approaches have not yet been used in the literature for diagram evaluation, though Gregory quadratures up to order $p = 6$ have been used in nonequilibrium Green's function calculations for real and imaginary time integrals [76]. Other possibilities include spectral methods like Gauss quadrature, yielding spectral accuracy, or composite spectral methods, yielding arbitrarily high-order accuracy, but these rules are not based on an underlying equispaced grid and therefore require on-the-fly evaluation of the integrand on irregular grids.

D. Discrete Lehmann representation

We give a short summary of the main properties of the DLR used by our algorithm. For a detailed description of

the DLR, we refer to Ref. [48], and to Ref. [80] for another brief overview. The DLR, like the closely related intermediate representation (IR) [81,82], is based on the spectral Lehmann representation

$$G(\tau) = -\int_{-\infty}^{\infty} d\omega K(\tau,\omega)\rho(\omega) \tag{19}$$

of imaginary-time Green's functions. Here, G is the Green's function, ρ is its integrable spectral function, and

$$K(\tau,\omega) = \frac{e^{-\tau\omega}}{1+e^{-\beta\omega}} \tag{20}$$

is called the analytic continuation kernel. Given the support constraint $\rho(\omega) = 0$ for ω outside $[-\omega_{\max}, \omega_{\max}]$ and defining $\Lambda = \beta\omega_{\max}$ as above, one observes that the singular values of the integral operator defining the representation (19) decay superexponentially. In particular, the ε-rank r—the number of singular values larger than ε—is $\mathcal{O}(\log(\Lambda)\log(1/\varepsilon))$. This finding implies that the image of the operator, which contains all imaginary-time Green's functions, can be characterized to accuracy ε by a basis of only $r = \mathcal{O}(\log(\Lambda)\log(1/\varepsilon))$ functions.

Taking these functions to be the left singular vectors of the operator yields the orthogonal IR basis. Alternatively, taking the functions to be $K(\tau,\omega_l)$ for r carefully chosen ω_l yields the nonorthogonal but explicit DLR basis. In particular, it is shown in Ref. [48] that the DLR frequencies ω_l can be selected, using rank-revealing pivoted Gram-Schmidt orthogonalization, to give the DLR expansion

$$G(\tau) \approx \sum_{l=1}^{r} K(\tau,\omega_l)\hat{g}_l \tag{21}$$

accurate to ε, with r possibly slightly larger than the ε rank of the operator, or the number of its singular values greater than ε. We emphasize that r and the DLR frequencies depend only on Λ and ε, and not on $G(\tau)$ itself; to ε accuracy, the span of the DLR basis contains all imaginary-time Green's functions satisfying the user-specified cutoff Λ.

Using a similar pivoted Gram-Schmidt procedure, one can construct a set of r DLR interpolation nodes τ_k such that the DLR coefficient $\hat{g}_l$ can be stably recovered from samples $G(\tau_k)$ by solving the $r \times r$ linear system

$$G(\tau_k) = \sum_{l=1}^{r} K(\tau_k,\omega_l)\hat{g}_l.$$

This process is similar to the sparse sampling method [83], typically used in conjunction with the IR basis, which obtains stable interpolation grids from the extrema of the highest-degree IR basis function. Green's functions can then be represented by their values on this DLR grid, and operations can be carried out using this representation. For example, given Green's functions $F(\tau)$ and $G(\tau)$ represented by their DLR grid samples $F(\tau_k)$ and $G(\tau_k)$, we can evaluate their product $H = FG$ on the DLR grid, $H(\tau_k) = F(\tau_k)G(\tau_k)$. Then, the DLR expansion of H can be obtained as described above. An efficient algorithm to compute the convolution $H(\tau) = \int_0^\beta d\tau' F(\tau-\tau')G(\tau')$ or time-ordered convolution $H(\tau) = \int_0^\tau d\tau' F(\tau-\tau')G(\tau')$ is described in Appendix A. We note that our method assumes self-energies and hybridization functions, as well as products and convolutions of DLR expansions, can be represented accurately in the DLR basis, which has been observed to be the case in many previous works [48,83–89].

IV. EFFICIENT EVALUATION OF IMAGINARY-TIME DIAGRAMS

Our algorithm improves the $\mathcal{O}(\Lambda^{2M-1})$ scaling of the standard equispaced integration method described in Sec. III C to $\mathcal{O}((2M-2)r^{M+1}) = \mathcal{O}((2M-2)(\log\Lambda)^{M+1})$. It exploits the separability of the analytic continuation kernel and therefore the DLR basis functions:

$$K(\tau-\tau',\omega) = \frac{K(\tau,\omega)K(\tau',-\omega)}{K(0,-\omega)}. \tag{22}$$

Using Eq. (22), we can separate variables in the hybridization functions which break the convolutional structure of the backbone, reducing diagrams to sums over nested products and convolutions. Each such operation can then be evaluated efficiently in the DLR basis, as described above.

We first demonstrate the technique using the OCA-type self-energy diagram (18). Replacing Δ_2 by its DLR expansion $\Delta_2(\tau) = \sum_{l=1}^{r} K(\tau,\omega_l)\hat{\Delta}_{2l}$ and separating variables gives

$$\Delta_2(\tau-\tau_1) = \sum_{l=1}^{r} \frac{K(\tau,\omega_l)K(\tau_1,-\omega_l)}{K(0,-\omega_l)}\hat{\Delta}_{2l}, \tag{23}$$

and inserting this expression into Eq. (18) gives

$$\Sigma(\tau) = \sum_{l=1}^{r} \frac{\hat{\Delta}_{2l}}{K(0,-\omega_l)} K(\tau,\omega_l) \int_0^\tau d\tau_2 \mathcal{G}_3(\tau-\tau_2)\Delta_1(\tau_2) \times \int_0^{\tau_2} d\tau_1 \mathcal{G}_2(\tau_2-\tau_1)\mathcal{G}_1(\tau_1)K(\tau_1,-\omega_l). \tag{24}$$

Each term of the sum now consists of a nested sequence of one-dimensional products and convolutions, which can be evaluated by the following procedure: (1) Multiply $\mathcal{G}_1$ and $K(\cdot,-\omega_l)$, (2) convolve by $\mathcal{G}_2$,

(3) multiply by Δ_1, (4) convolve by $\mathcal{G}_3$, and (5) multiply by $[\hat{\Delta}_{2l}/K(0,-\omega_l)]K(\cdot,\omega_l)$. Here, products can be taken pointwise on the DLR grid of r nodes, and convolutions can be computed at an $\mathcal{O}(r^2)$ cost using the method described in Appendix A.

A final technical point on numerical stability must be addressed. Since $1/K(0,-\omega_l) = 1 + e^{\beta\omega_l}$, Eq. (24) is vulnerable to overflow if $\omega_l > 0$. In this case, we can rewrite Eq. (23) using

$$K(\tau-\tau',\omega) = \frac{K(\tau-\tau'',\omega)K(\tau''-\tau',\omega)}{K(0,\omega)} \tag{25}$$

in place of Eq. (22) to obtain

$$\Delta_2(\tau-\tau_1) = \sum_{\omega_l\le 0}\frac{K(\tau,\omega_l)K(\tau_1,-\omega_l)}{K(0,-\omega_l)}\hat{\Delta}_{2l} + \sum_{\omega_l>0}\frac{K(\tau-\tau_2,\omega_l)K(\tau_2-\tau_1,\omega_l)}{K(0,\omega_l)}\hat{\Delta}_{2l}. \tag{26}$$

This process gives a numerically stable replacement of Eq. (24):

$$\begin{aligned}\Sigma(\tau) = {}& \sum_{\omega_l\le 0}\frac{\hat{\Delta}_{2l}}{K_l^-(0)}K_l^+(\tau)\int_0^\tau d\tau_2\mathcal{G}_3(\tau-\tau_2)\Delta_1(\tau_2)\\ & \times\int_0^{\tau_2} d\tau_1\mathcal{G}_2(\tau_2-\tau_1)(\mathcal{G}_1K_l^-)(\tau_1)\\ & + \sum_{\omega_l>0}\frac{\hat{\Delta}_{2l}}{K_l^+(0)}\int_0^\tau d\tau_2(\mathcal{G}_3K_l^+)(\tau-\tau_2)\Delta_1(\tau_2)\\ & \times\int_0^{\tau_2} d\tau_1(\mathcal{G}_2K_l^+)(\tau_2-\tau_1)\mathcal{G}_1(\tau_1).\end{aligned} \tag{27}$$

Here, we have introduced the notation

$$K_l^\pm(\tau) \equiv K(\tau,\pm\omega_l) \tag{28}$$

and

$$(\mathcal{G}_iK_l^\pm)(\tau) \equiv \mathcal{G}_i(\tau)K(\tau,\pm\omega_l). \tag{29}$$

The procedure to evaluate the terms with $\omega_l \le 0$ is the same as above, but for those with $\omega_l > 0$, it is slightly modified: (1) Multiply $\mathcal{G}_2$ and K_l^+, (2) convolve the result with $\mathcal{G}_1$, (3) multiply by Δ_1, (4) multiply $\mathcal{G}_3$ and K_l^+, (5) convolve with the previous result, and (6) multiply by $\hat{\Delta}_{2l}/K_l^+(0)$.

A. General procedure

This idea may be generalized to arbitrary Mth-order pseudoparticle self-energy and single-particle Green's function diagrams, containing internal time integration variables $\tau_1,\ldots,\tau_{2M-2}$, using the following procedure. Let Δ correspond to a hybridization line which does not connect to time zero, with DLR coefficients $\hat{\Delta}_l$. Order all imaginary-time variables, including the variable τ, as $\tau_1' \le \tau_2' \le \cdots \le \tau_{2M-1}'$. Thus, for the self-energy diagrams, we have $\tau_i = \tau_i'$ for $i = 1,\ldots,2M-2$, and $\tau_{2M-1}' = \tau$. For the Green's function diagrams, we have some $k < 2M-1$ such that $\tau_i' = \tau_i$ for $i = 1,\ldots,k-1$, $\tau_k' = \tau$, and $\tau_i' = \tau_{i-1}$ for $i = k+1,\ldots,2M-1$. Replace $\Delta(\tau_i'-\tau_j')$ with

$$\begin{aligned}\Delta(\tau_i'-\tau_j') = {}& \sum_{\omega_l\le 0}\frac{\hat{\Delta}_l}{K_l^-(0)}K_l^+(\tau_i')K_l^-(\tau_j')\\ & + \sum_{\omega_l>0}\frac{\hat{\Delta}_l}{(K_l^+(0))^{i-j-1}}K_l^+(\tau_i'-\tau_{i-1}')K_l^+(\tau_{i-1}'-\tau_{i-2}')\\ & \cdots K_l^+(\tau_{j+1}'-\tau_j').\end{aligned} \tag{30}$$

If this procedure is followed for all such hybridization lines, the resulting expression can be rearranged into sums over nested sequences of products and convolutions. The hybridization line connecting to time zero (e.g., Δ_1 in the example above) is excluded because the corresponding hybridization function only depends on a single time variable and therefore does not break the convolutional structure of the backbone.

Let us analyze the cost of this procedure. We ignore the $\mathcal{O}(r)$ cost of products since the $\mathcal{O}(r^2)$ cost of convolutions dominates. Each hybridization line that is decomposed yields a sum over r frequencies ω_l, so we obtain a sum over r^{M-1} terms. Each such term contains one convolution for each of the $2M-2$ internal time variables, yielding an $\mathcal{O}((2M-2)r^2)$ complexity per term or an $\mathcal{O}((2M-2)r^{M+1}) = \mathcal{O}((2M-2)(\log(\Lambda)\log(1/\varepsilon))^{M+1})$ complexity in total.

We note that a similar procedure can be applied to the weak coupling expansion, with minor modifications. This procedure is described in detail in Appendix C.

Remark 3. Although we use the DLR expansion to decompose the hybridization functions, this is not strictly necessary. Rather, one could expand each hybridization function as an arbitrary sum of exponentials, $\Delta(\tau) \approx \sum_{l=1}^p K(\tau,\omega_l^\Delta)\hat{\Delta}_l$, tailored to Δ so that $p < r$, and apply the same scheme. This process would yield the improved complexity $\mathcal{O}((2M-2)r^2p^{M-1})$. Formulated in the Matsubara frequency domain, this gives a rational approximation problem that has been studied for a variety of applications in many-body physics, and several approaches have been proposed [1,90–92]. We use the DLR expansion in the present work for simplicity and will revisit the

problem of a more optimal sum-of-exponentials expansion in future work.

B. Example: OCA diagram for single-particle Green's function

To further illustrate the general procedure, we consider the OCA diagram for the single-particle Green's function, which takes the form

$$G(\tau) = \int_\tau^\beta d\tau_2 \Delta(\tau_2 - \tau_1)\mathcal{G}_4(\beta - \tau_2)\mathcal{G}_3(\tau_2 - \tau) \times \int_0^\tau d\tau_1 \mathcal{G}_2(\tau - \tau_1)\mathcal{G}_1(\tau_1). \tag{31}$$

For simplicity, we suppress the trace appearing in the single-particle Green's function diagrams, e.g., in Eq. (16). In the notation of Eq. (30), we have $\tau_1' = \tau_1$, $\tau_2' = \tau$, and $\tau_3' = \tau_2$. Separating variables in $\Delta(\tau_2 - \tau_1)$ and using the identity $K(\tau, \omega) = K(\beta - \tau, -\omega)$, we obtain

$$\begin{aligned} G(\tau) = &\sum_{\omega_l \le 0} \frac{\hat{\Delta}_l}{K_l^-(0)} \int_\tau^\beta d\tau_2 (\mathcal{G}_4 K_l^-)(\beta - \tau_2)\mathcal{G}_3(\tau_2 - \tau) \\ &\times \int_0^\tau d\tau_1 \mathcal{G}_2(\tau - \tau_1)(\mathcal{G}_1 K_l^-)(\tau_1) \\ &+ \sum_{\omega_l > 0} \frac{\hat{\Delta}_l}{K_l^+(0)} \int_\tau^\beta d\tau_2 \mathcal{G}_4(\beta - \tau_2)(\mathcal{G}_3 K_l^+)(\tau_2 - \tau) \\ &\times \int_0^\tau d\tau_1 (\mathcal{G}_2 K_l^+)(\tau - \tau_1)\mathcal{G}_1(\tau_1). \end{aligned} \tag{32}$$

Time-ordered convolutions of the form $\int_\tau^\beta d\tau' f(\beta - \tau')g(\tau' - \tau)$ can be reduced to the standard form introduced above by a change of variables and a reflection operation, as described in Appendix A.

A final example for a third-order pseudoparticle self-energy diagram is given in Appendix B.

V. DIAGRAMMATIC FORMULATION OF THE ALGORITHM

Our procedure can be expressed diagrammatically, which significantly simplifies its implementation. From Eq. (30), we see that the terms $\omega_l \le 0$ can be expressed by replacing each hybridization line by a line connecting $\tau = \tau_i$ and $\tau = 0$, labeled by K_l^+, and a line connecting $\tau = 0$ and $\tau = \tau_j$, labeled by K_l^-. The terms $\omega_l > 0$ can be expressed by replacing each hybridization line by a chain of lines: one connecting $\tau = \tau_i$ to $\tau = \tau_{i-1}$, one connecting $\tau = \tau_{i-1}$ to $\tau = \tau_{i-2}$, and so on, all labeled by K_l^+. For the OCA diagram (18), for example, we obtain

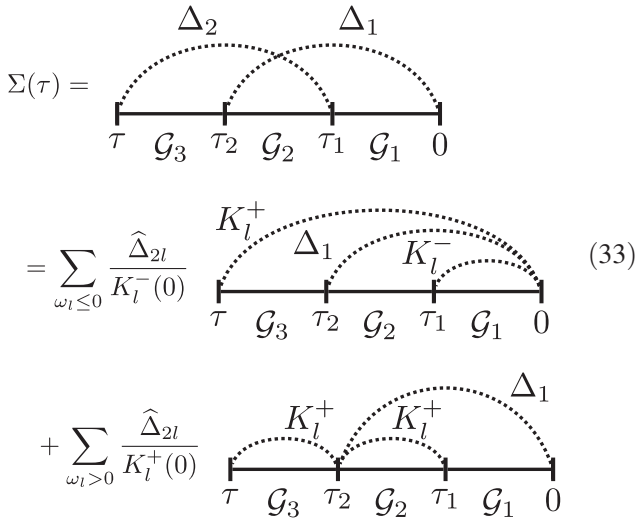

(33)

which reproduces Eq. (27).

This diagrammatic notation can be simplified by observing that lines connecting to $\tau = 0$ represent a multiplication rather than a convolution, and that all lines connecting adjacent time variables can be absorbed into the backbone line connecting those time variables. The above can therefore be replaced by the shorthand

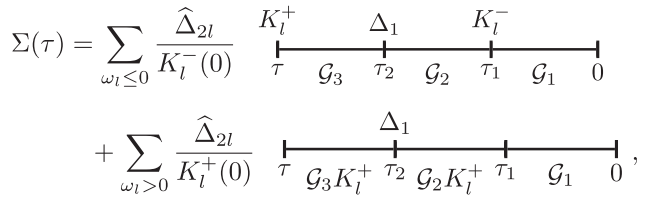

(34)

where vertical lines centered at a given time variable represent multiplication by the indicated function, and the functions attached to backbone lines have been suitably modified. This shorthand notation emphasizes the central idea of our algorithm: that diagrams can be reduced to sums over backbone diagrams with a simple convolutional structure.

Using this shorthand, the single-particle Green's function OCA diagram (31) is decomposed as

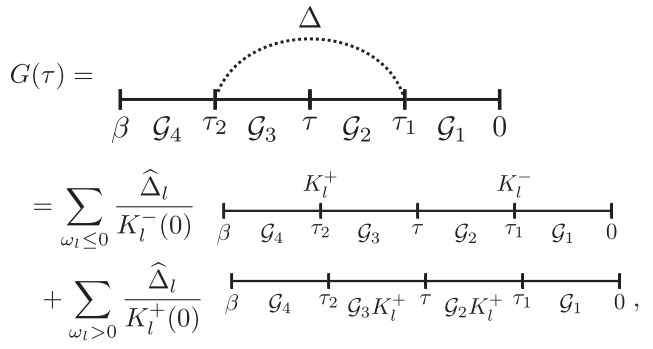

(35)

which reproduces Eq. (32) upon use of the identity $K(\tau,\omega) = K(\beta-\tau,-\omega)$.

The diagrammatic procedure is illustrated for a third-order self-energy diagram in Appendix B.

VI. NUMERICAL EXAMPLES

We demonstrate an implementation of our algorithm in a strong-coupling expansion solver including all self-energy and single-particle Green's function diagrams up to third order. While our procedure can be applied to diagrams of arbitrary order, in our calculations we have constructed all decompositions by hand, limiting the order in practice. However, this is a technical limitation, which can be overcome by a code implementing the procedure described in Secs. IV and V in an automated manner. All calculations used libdlr for the implementation of the DLR [80,93].

We apply our solver to benchmark systems for which the continuous time hybridization expansion quantum Monte Carlo method (CT-HYB) [2,29–31] exhibits a severe sign problem [42–44] due to nonzero off-diagonal hybridization or off-diagonal local hopping in the impurity model.

A. Fermion dimer

To establish the correctness and order-by-order convergence of our strong-coupling solver, we begin by solving impurity models with discrete, finite baths. These systems can be diagonalized exactly, yielding a numerically exact reference for the single-particle Green's function. We first consider a two-orbital spinless model with interorbital hopping, coupled to a discrete bath with off-diagonal hybridization. This minimal model was also used as a benchmark in Ref. [42]. Its Hamiltonian has the form

$$H = Uc_0^\dagger c_0 c_1^\dagger c_1 - v(c_0^\dagger c_1 + c_1^\dagger c_0) - t\sum_{k=0}^{1}\sum_{i=0}^{1}(c_i^\dagger b_{ik} + \text{H.c.}) - t'\sum_{k=0}^{1}(b_{0k}^\dagger b_{1k} + \text{H.c.}), \tag{36}$$

where c_i is the annihilation operator for the impurity states ($i \in \{0,1\}$) and b_{ik} is the annihilation operator for the bath states $k \in \{0,1\}$ coupled to the ith impurity state. Note that U is the impurity interaction parameter, v is the interorbital hopping parameter, t is the parameter for the direct hopping between the impurity and bath orbitals, and t' is the parameter for the interbath hopping, which generates an off-diagonal hybridization.

Following Ref. [42], we use the parameters $t = 1$, $U = 4t$, $v = 3t/2$, and $t' = 3t/2$. In Fig. 1, we compare our strong-coupling expansion results for the diagonal (G_{00}) and off-diagonal (G_{01}) single-particle Green's function at first, second, and third order to the exact solution, for $\beta = 2$, 16, 128, and 1024. We use the DLR parameters $\Lambda = 20\beta$ and $\varepsilon = 10^{-12}$, yielding 26, 47, 71, and 93 basis

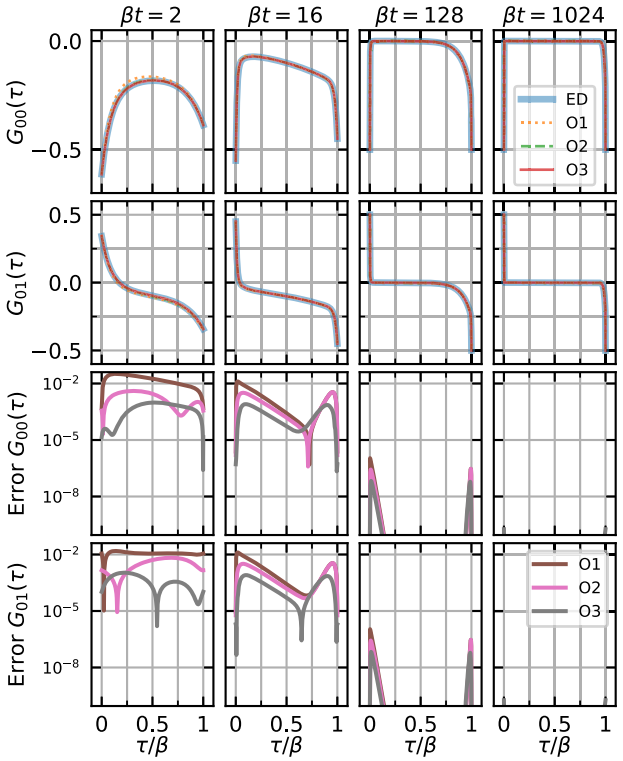

FIG. 1. Single-particle Green's function for the spinless fermion dimer model (36), at inverse temperatures $\beta t = 2$, 16, 128, 1024 (columns), and increasing expansion orders. The exact diagonal (first row) and off-diagonal (second row) Green's functions obtained from exact diagonalization (ED) are quantitatively described by the first-order approximation (O1). The diagonal (third row) and off-diagonal (last row) Green's function error decreases when increasing to second (O2) and third (O3) order.

functions, respectively. The pseudoparticle self-consistency is iterated until the maximum absolute change in $\mathcal{G}(\tau)$ is less than 10^{-9}, requiring fewer than 12 iterations (with higher temperatures exhibiting slower convergence). At second order, there are 64 pseudoparticle self-energy and 32 single-particle Green's function diagrams. At third order, there are 2048 pseudoparticle self-energy diagrams (of which 896 are nonzero) and 1024 single-particle Green's function diagrams (of which 448 are nonzero). These numbers account for diagram topologies, hybridization insertions, and forward or backward propagation. The diagram evaluations are independent, enabling perfect parallel scaling.

The error shows an order-by-order convergence and a rapid decrease as the temperature is lowered. The decrease in the error with temperature is a consequence of the "freezing-out" of the discrete bath degrees of freedom. These results demonstrate that a direct diagram evaluation approach is useful for systems in the strong-coupling limit even when limited to third order. At $\beta = 2$ with $r = 26$, our third-order calculations require fewer than 0.2 core hours (for nine self-consistent iterations), and at $\beta = 1024$ with

$r = 93$, the same calculation takes 4.4 core hours (for two iterations). These timings can be compared with the 500 core hours reported for the inchworm Monte Carlo method in Ref. [42] for the same system (for $\beta = 4$–64), though the errors in our third-order calculations are smaller than the stochastic noise shown there in Fig. 1.

B. Two-band Anderson impurity model

The two-band Anderson impurity model is relevant for the description of correlated e_g bands in transition metal systems. The local Coulomb interaction has the Kanamori form [94]

$$H_{\mathrm{loc}} = U \sum_{\kappa \in \{0,1\}} n_{\kappa\downarrow} n_{\kappa\uparrow} + \sum_{\kappa<\lambda,\sigma\sigma'} (U' - J_H \delta_{\sigma\sigma'}) n_{\kappa\sigma} n_{\lambda\sigma'} + J_H \sum_{\kappa\neq\lambda} \left(c^\dagger_{\kappa\uparrow} c^\dagger_{\kappa\downarrow} c_{\lambda\downarrow} c_{\lambda\uparrow} + c^\dagger_{\kappa\uparrow} c^\dagger_{\lambda\downarrow} c_{\kappa\downarrow} c_{\lambda\uparrow} \right), \tag{37}$$

with Hubbard interaction U, $U' = U - 2J_H$, and Hund's coupling J_H. The Hund's coupling favors high-spin states and has an important effect on the ordered phases [95] and the dynamics of orbital and spin moments [96]. To enable comparison with exact results, we follow Ref. [42] and consider the two-band impurity model coupled to a bath with an off-diagonal hybridization given by $\Delta_{\kappa\lambda}(\omega) = [\delta_{\kappa\lambda} + s(1-\delta_{\kappa\lambda})] t^2 \tilde{\mathcal{G}}(\omega)$, where s controls the off-diagonal coupling. We consider two cases: a discrete bath, and a bath with a continuous semicircular spectral function.

In the first case, we use a single bath site per orbital. The hybridization function is given by $\tilde{\mathcal{G}}(\omega) = \sum_k \delta(\omega - \epsilon_k)$ with $\epsilon_k \in \{\pm 2.3t\}$, and we use a strong off-diagonal hybridization $s = 1/2$. This case can be solved using exact diagonalization, and it provides a nontrivial test. The rapid order-by-order convergence of the orbitally resolved Green's function $G_{\lambda\kappa}(\tau - \tau') = -\langle c_\lambda(\tau) c^\dagger_\kappa(\tau') \rangle$ computed by our strong-coupling solver is shown in Fig. 2 at $\beta = 2$, 16, 128, and 1024. We use the DLR parameters $\Lambda = 12.5\beta$ and $\varepsilon = 10^{-8}$, yielding 17, 32, 46, and 61 basis functions, respectively. The pseudoparticle self-consistency is iterated until the maximum absolute change in $\mathcal{G}(\tau)$ is less than 10^{-6}, requiring fewer than 12 iterations for the temperatures and expansion orders considered. At second order, there are 256 pseudoparticle self-energy and 64 single-particle Green's function diagrams. At third order, there are 16,384 pseudoparticle self-energy diagrams (of which 14,080 are nonzero), and 4096 single-particle Green's function diagrams (of which 3520 are nonzero).

As in the fermion dimer example, the error decreases with the temperature. Interestingly, the results show that the off-diagonal component $G_{01}(\tau)$ becomes substantially enhanced at lower temperatures, with sharp features emerging around $\tau = 0$ and $\tau = \beta$. Physically, these features correspond to short-time quantum fluctuations between orbitals and should be important for the stabilization of orbital orders. The DLR discretization of the Green's function is able to capture such features significantly more efficiently than a standard equispaced grid discretization.

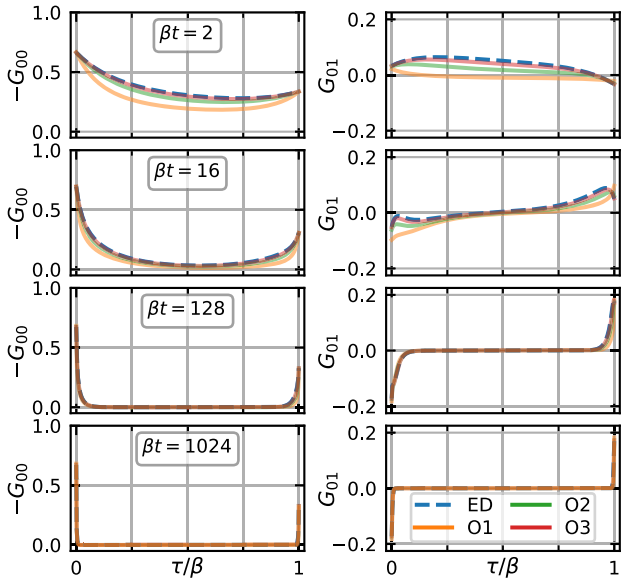

FIG. 2. Single-particle Green's function for the two-band e_g model with a discrete bath. The left column shows the diagonal Green's function $G_{00}(\tau)$, and the right column shows the off-diagonal component $G_{01}(\tau)$, with decreasing temperatures $\beta t = 2$, 16, 128, and 1024 along the rows. The strong-coupling results converge to the ED solution as the expansion order increases.

We next present results for the metallic semicircular hybridization function given by $\tilde{\mathcal{G}}(\omega) = (2/\pi D^2)\sqrt{D^2 - \omega^2}$, with $s = 1$ and $D = 2t$, at inverse temperature $\beta = 8/t$. We use the DLR parameters $\lambda = 10\beta$ and $\varepsilon = 10^{-10}$, yielding 25 basis functions. The pseudoparticle self-consistency converges below 10^{-6} in fewer than 30 iterations. In Fig. 3, we compare our approach with the inchworm Monte Carlo [42,45,97] and CT-HYB [2,29–31] methods, using the

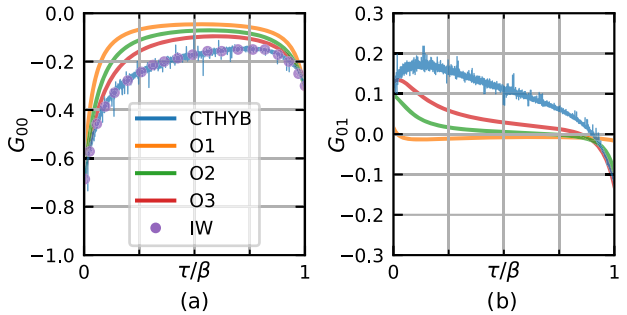

FIG. 3. Single-particle Green's function for the two-band e_g model with a metallic bath at inverse temperature $\beta t = 8$. The diagonal part G_{00} is shown in panel (a), and the off-diagonal part G_{01} in panel (b). The strong-coupling expansion converges towards the result produced by the CT-HYB method and the inchworm quantum Monte Carlo (IW) results from Ref. [42], but in this case, diagrams beyond third order contribute significantly.

TRIQS [98] implementation [99] for the latter. For CT-HYB, the average sign is approximately 0.25, and reducing the variance is costly, though techniques such as improved estimators [100–102] and worm sampling [103,104] could, in principle, mitigate this difficulty. However, the exponential decay of the sign with temperature severely restricts this method. The inchworm algorithm does not suffer the same kind of sign problem [42,45], and inchworm Monte Carlo results down to $t\beta = 64$ have been reported [42].

While our strong-coupling solver still converges with the order, the third-order solution differs significantly from the exact solution. This system lies outside the reach of a third-order strong-coupling expansion, as is expected since the model is far from the strong-coupling limit and would require the inclusion of higher-order diagrams. We note, however, that our result was obtained at a significantly lower cost than the corresponding inchworm calculation (154 core hours vs 1500 core hours at $t\beta = 8$), so including higher-order diagrams within our framework should be tested for comparison.

C. Minimal model for Ca_2RuO_4

Our previous results suggest that the strong-coupling expansion converges rapidly in the insulating regime. For many insulating systems, like Mott insulators with tetragonal symmetry and strong spin-orbit coupling, off-diagonal hybridization plays an important role. This case represents a substantial challenge for Monte Carlo-based solvers, due to the sign problem. The most promising work-around was introduced in Ref. [44], which used the interaction expansion in combination with a basis rotation to reduce the sign problem and enable an analysis of a spin-orbit coupled system at elevated temperatures. We have seen that the strong-coupling expansion proposed in this work is easily extendable to spin-orbit coupled systems as long as the system is deep within the Mott insulating phase. Here, we provide a proof-of-principle calculation for a minimal model of Ca_2RuO_4 [43,49,105].

The electronic configuration of Ca_2RuO_4 includes four electrons in the three t_{2g} orbitals, which, at low temperatures, undergo an isosymmetric structural transition accompanied by a Mott metal-insulator transition. This structural distortion reduces the energy of the d_{xy} orbital, making it doubly occupied. The remaining orbitals with two electrons undergo a Mott metal-insulator transition, leading to the $S = 1$ state [49,51,105]. In the t_{2g} space, the matrix representation of the orbital moment operators is (up to a sign) equal to the $L = 1$ operator in the cubic basis, an observation that is often called TP correspondence [106]. An open question is the nature of the magnetic moments due to strong spin-orbit coupling. Two scenarios were proposed in the literature: (i) The spin-orbit coupling leads to a correction of the $S = 1$ picture and induces a single-ion anisotropy [43], and (ii) the spin-orbit coupling changes the moment of the ground state to $j_{\mathrm{eff}} = 0$ [107,108]. It is difficult to distinguish these two scenarios *a priori* from the value of the spin-orbit coupling, as its effect can be substantially enhanced due to a dynamical increase of the spin-orbit effect. Answering these questions therefore requires unbiased simulations. Our goal is not to solve the question of Ca_2RuO_4 but rather to show that, on the level of the minimal model, we can capture the competition between all relevant interactions. We leave the extension of our approach to full *ab initio* models, and the resolution of the question of magnetism in Ca_2RuO_4 as an important future problem.

We consider a three-orbital Hubbard model spanned by d_{xy}, d_{xz}, and d_{yz} orbitals within the DMFT approximation, which maps the lattice problem to an impurity problem. The local part of the impurity problem is given by

$$\begin{aligned} H_{\mathrm{loc}} = H_{\mathrm{LS}} &+ \sum_{\kappa\sigma}[\epsilon_\kappa - \mu]c^\dagger_{\kappa\sigma}c_{\kappa\sigma} + U\sum_{\kappa} n_{\kappa\uparrow}n_{\kappa\downarrow} \\ &+ \sum_{\kappa<\lambda}\sum_{\sigma,\sigma'}(U' - J_H\delta_{\sigma\sigma'})n_{\kappa\sigma}n_{\lambda\sigma'} \\ &+ J_H\sum_{\kappa\neq\lambda}\left(c^\dagger_{\kappa\uparrow}c^\dagger_{\kappa\downarrow}c_{\lambda\downarrow}c_{\lambda\uparrow} + c^\dagger_{\kappa\uparrow}c^\dagger_{\lambda\downarrow}c_{\kappa\downarrow}c_{\lambda\uparrow}\right), \end{aligned} \tag{38}$$

where $\kappa, \lambda \in \{d_{xy}, d_{xz}, d_{yz}\}$, and the on-site energies $\epsilon_{xz} = \epsilon_{yz} = 0$ are split with respect to the doubly occupied d_{xy} orbital by the crystal field $\epsilon_{xy} = \Delta_{\mathrm{cf}} = -0.5$ eV. We choose the chemical potential μ such that the system is occupied by four electrons on average. The interacting part of the Hamiltonian is given by the Slater-Kanamori interaction parametrized by the Hubbard interaction U and the Hund's coupling J_H. We use the established values $U = 2.3$ eV and $J_H = 0.4$ eV obtained from the constrained random phase approximation [43,49,109]. The spin-orbit coupling introduces a complex coupling between the t_{2g} orbitals. By employing the TP correspondence, we obtain

$$H_{\mathrm{LS}} = \lambda_{\mathrm{SOC}}\vec{L}\cdot\vec{S} = \frac{\mathrm{i}\lambda_{\mathrm{SOC}}}{2}\sum_{\kappa\lambda\mu,\sigma\sigma'}\epsilon_{\kappa\lambda\mu}\tau^\mu_{\sigma\sigma'}c^\dagger_{\kappa\sigma}c_{\lambda\sigma'}, \tag{39}$$

where $\lambda_{\mathrm{SOC}} = 0.1$ eV is the size of the spin-orbit coupling, ϵ is the Levi-Civita matrix element, and τ^ν is the νth Pauli matrix.

We solve the problem on the Bethe lattice, for which the DMFT self-consistency condition is particularly simple. The hybridization function $\Delta_{\lambda\kappa}$ is obtained from the local Green's function $G_{\lambda\kappa}(\tau - \tau') = -\langle \mathcal{T} c_\lambda(\tau)c^\dagger_\kappa(\tau')\rangle$ as $\Delta_{\lambda\kappa} = t_\lambda G_{\lambda\kappa} t_\kappa$. We restrict to intra-orbital transitions given by $t_\lambda = \{t_{d_{xy}}, t_{d_{xz}}, t_{d_{yz}}\}$, and the hopping integrals are estimated as $t_{d_{yz}} = t_{d_{xz}} = 0.25$ eV and $t_{d_{xy}} = 0.5$ eV to match the bandwidth measured by ARPES and previous theoretical studies [49]. All calculations are performed at inverse temperature $\beta = 10$ eV^{-1}.

To our knowledge, ours is the first self-consistent third-order strong-coupling DMFT calculation for a three-band model. We use the DLR parameters $\Lambda = 100$ and $\varepsilon = 10^{-8}$, yielding 26 basis functions. We perform the pseudoparticle self-energy and DMFT lattice self-consistencies in tandem, with a tolerance threshold of 10^{-6} for changes in the respective propagators, requiring 11 iterations for the first-order calculation, nine iterations for the second-order calculation, and seven iterations for the third-order calculation. At each order, we use the solution from the previous order for the initial iterate. The calculation took approximately 90,000 core hours (11 hours on 8192 cores) using our preliminary code, with the independent evaluation of 186,624 third-order diagrams performed in parallel. Although the use of the DLR enables efficient diagram evaluation at very low temperatures, we find that the convergence of the DMFT and pseudoparticle self-consistency exhibits a critical slow-down as the temperature is lowered. We attribute this finding to the presence of the antiferromagnetic instability of the two half-filled orbitals, as observed in Ca_2RuO_4, which becomes antiferromagnetic at the Néel temperature $T_N \approx 110$ K [110].

We plot the diagonal part of the single-particle propagator $G_{\alpha\alpha}$ for $\alpha \in \{d_{xy}, d_{xz}, d_{yz}\}$ in Fig. 4(a). We observe that the d_{xy} orbital is almost fully occupied, and the d_{xz} and d_{yz} orbitals are half filled due to the strong Coulomb interaction. In agreement with the previous examples, we observe rapid convergence with increasing diagram order. We observe a maximum absolute difference between the second- and third-order calculations of less than 6×10^{-3}, which gives a reasonable estimate of the error in the second-order calculation. Thus, the third-order calculation not only gives us a more accurate result, but it also allows us to estimate the error of the second-order calculation. The main effect of the higher-order diagrams is to enhance the value of the propagators away from the edges of the interval $[0, \beta]$, which we interpret as an increase in charge fluctuations with the increasing order of the expansion. These results allow us to estimate the orbital polarization $p = n_{xy} - (n_{xz} + n_{yz})/2$, which, in the system with finite spin-orbit coupling, is given by $p = 0.84$ and is similar to the result without the spin-orbit coupling, $p_{\lambda=0} = 0.87$. This finding is consistent with the conclusion of Ref. [43], in which the persistence of strong orbital polarization upon inclusion of the spin-orbit coupling was used as a signature of the $S = 1$ picture. While the spin-flip and pair-hopping terms were neglected in Ref. [43], our results confirm that at the level of the minimal model, their effect would not produce a significant qualitative change.

Because of the spin-orbit coupling, the single-particle propagators $G_{\lambda\kappa}$ obtain complex off-diagonal components, as shown in Fig. 4(b) for Im $G_{xz\sigma,yz\sigma}(\tau)$ and in Fig. 4(c) for Re $G_{xz\sigma,xy\bar{\sigma}}(\tau)$. Hence, the spin-orbit coupling also generates a dynamic mixing of spin and orbitals, coupling the out-of-plane orbitals xz and yz for equal spin and the in-plane orbital xy with the spin-flipped component of the out-of-plane orbitals. This result can be understood from the structure of the spin-orbit coupling in the t_{2g} subspace of the d-orbital cubic harmonics [111]. It is the sign change in these off-diagonal components as a function of τ that generates a dynamical sign problem in the hybridization determinant of the CT-HYB algorithm [2,29–31].

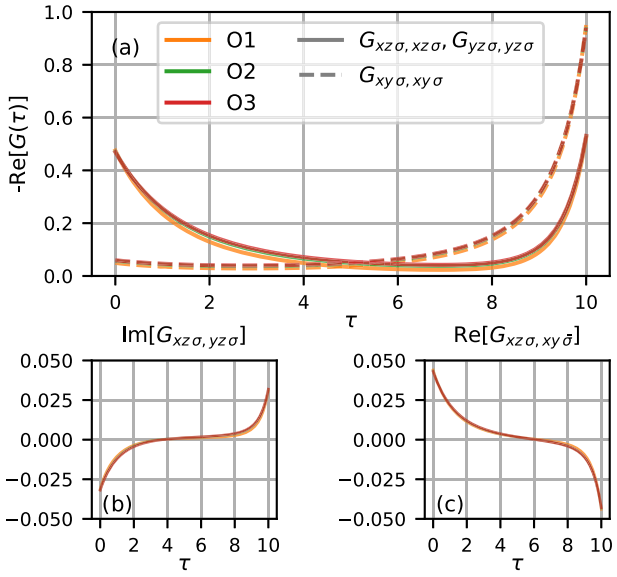

FIG. 4. (a) Diagonal component of the single-particle Green's function, with increasing expansion orders, for the three-band effective model of Ca_2RuO_4. Here, $G_{xz\sigma,xz\sigma}(\tau)$ and $G_{yz\sigma,yz\sigma}(\tau)$ are degenerate and close to half filling (solid lines), while $G_{xy\sigma,xy\sigma}(\tau)$ is close to unity filling (dashed lines). (b) Imaginary part of the off-diagonal component $G_{xz\sigma,yz\sigma}(\tau)$. (c) Real part of the off-diagonal component $G_{xz\sigma,xy\bar{\sigma}}(\tau)$ generated by the local spin-orbit coupling. Calculations were performed at inverse temperature $\beta = 10$ eV^{-1}.

Application of our method to realistic materials beyond our simplified proof-of-principle model would require an extension to a given lattice structure and combination with first-principles calculations, both well-established techniques. This application will be explored in our future work.

VII. CONCLUSION

We have proposed and implemented a new algorithm for the fast evaluation of imaginary-time Feynman diagrams. By taking advantage of a separability property of imaginary-time objects, the algorithm obtains a decomposition which can be evaluated efficiently within the DLR basis. We have developed the method in detail for the bold strong-coupling expansion of the Anderson impurity model, and we showcased an implementation up to third order. Its application to the weak coupling expansion is described in Appendix C. The extension to higher-order diagrams is straightforward and will be pursued in future work. A

parallel implementation of our algorithm provides a path towards robust and high-order accurate evaluation of diagrams at least up to intermediate orders at very low temperature, with no Monte Carlo integration and no sign problem. The combination of our approach with methods for diagrammatic expansions of very high order, including Monte Carlo [2,15] and TCI [46,47], is a topic of our current research. In particular, TCI might be used to exploit compressibility across imaginary-time and orbital degrees of freedom while maintaining the robustness, high-order accuracy, and favorable scaling at low temperatures of our scheme. In general, we expect the ideas presented here to serve as useful tools for future algorithmic development.

We envision that the ideal short-term applications of the proposed method are multiorbital systems within the Mott insulating regime involving strong off-diagonal hybridization terms induced by either spin-orbit coupling or symmetry-broken phases. Examples include Ca_2RuO_4 [43,49,105], Sr_2IrO_4 [112–115], and Nb_3Cl_8 [116]. In this limit, a reliable description is obtained by a relatively low-order expansion, but these systems are still challenging for current state-of-the-art Monte Carlo techniques due to the sign problem. A particularly appealing direction is to enter the symmetry-broken phase and study dynamical properties of exotic magnetic phases such as canted (anti)ferromagnetism [115]. The robustness, speed, and low memory footprint of our algorithm should allow it to couple well with *ab initio* descriptions based on DFT + DMFT in Mott insulators, as implemented in existing numerical libraries, e.g., TRIQS/DFTTools [117].

An efficient automated implementation of our algorithm, allowing for the evaluation of diagrams of arbitrary order and topology, is under development. Improvements to the algorithm, involving further decomposition of diagrams as well as more efficient representations of the hybridization function, are also being explored and are expected to yield significant further reductions in computational cost. Beyond imaginary-time diagrams, we believe the idea of fast diagram evaluation through compression of the integrand, either through separation of variables or otherwise, represents a promising research frontier with the potential to circumvent many of the limitations of traditional schemes.

ACKNOWLEDGMENTS

We thank O. Parcollet, A. Georges, R. Rossi, and G. Cohen for helpful discussions. Z. H. is supported by the Simons Investigator Award, which is a grant from the Simons Foundation (825053, Lin Lin). H. U. R. S. acknowledges funding from the European Research Council (ERC) under the European Union's Horizon 2020 research and innovation programme (Grant Agreement No. 854843-FASTCORR). Computations were enabled by resources provided by the National Academic Infrastructure for Supercomputing in Sweden (NAISS) and the Swedish National Infrastructure for Computing (SNIC) through Projects No. SNIC 2022/21-15, No. SNIC 2022/13-9, No. SNIC 2022/6-113, and No. SNIC 2022/1-18, at PDC, NSC, and CSC, partially funded by the Swedish Research Council through Grant Agreements No. 2022-06725 and No. 2018-05973. D. G. is supported by the Slovenian Research Agency (ARRS) under Programs No. J1-2455, No. MN-0016-106, and No. P1-0044. The Flatiron Institute is a division of the Simons Foundation.

APPENDIX A: FAST CONVOLUTION OF DLR EXPANSIONS

In Ref. [48], the imaginary-time convolution

$$H(\tau) = \int_0^\beta d\tau' F(\tau - \tau') G(\tau') \tag{A1}$$

is expressed in terms of the contraction of the vectors of values of F and G at the DLR nodes τ_k with a rank-three tensor: $H(\tau_i) = \sum_{j,k=1}^r C_{ijk} F(\tau_j) G(\tau_k)$. One can similarly write the time-ordered convolution

$$H(\tau) = \int_0^\tau d\tau' F(\tau - \tau') G(\tau') \tag{A2}$$

as a tensor contraction. The cost of this approach scales as $O(r^3)$. We demonstrate that these convolutions can be computed in only $\mathcal{O}(r^2)$ operations by writing the action of the convolution tensor on the DLR coefficients directly. We focus on Eq. (A2), but the method for Eq. (A1) is analogous.

Using the explicit formula (20), we first compute the time-ordered convolution (A2) of $K(\tau,\omega)$ and $K(\tau,\omega')$:

$$\int_0^\tau d\tau' K(\tau - \tau', \omega) K(\tau', \omega') = \begin{cases} \frac{K(0,\omega)K(\tau,\omega') - K(\tau,\omega)K(0,\omega')}{\omega - \omega'} & \omega \neq \omega' \\ \tau K(0,\omega) K(\tau,\omega) & \omega = \omega'. \end{cases} \tag{A3}$$

Given the DLR expansions $F(\tau) = \sum_{j=1}^r K(\tau,\omega_j)\widehat{f}_j$ and $G(\tau) = \sum_{k=1}^r K(\tau,\omega_k)\widehat{g}_k$, with possibly matrix-valued $\widehat{f}_j$ and $\widehat{g}_k$, this yields

$$\begin{aligned} H(\tau) &= \sum_{j,k=1}^{r} \widehat{f}_j \widehat{g}_k \int_0^\tau d\tau' K(\tau-\tau',\omega_j)K(\tau',\omega_k) \\ &= \tau \sum_{j=1}^{r} K(\tau,\omega_j)K(0,\omega_j)\widehat{f}_j \widehat{g}_j + \sum_{j=1}^{r} K(\tau,\omega_j)\left(\left(\sum_{\substack{k=1\\k\neq j}}^{r} \frac{K(0,\omega_k)}{\omega_k-\omega_j}\widehat{f}_k\right)\widehat{g}_j + \widehat{f}_j \sum_{\substack{k=1\\k\neq j}}^{r} \frac{K(0,\omega_k)}{\omega_k-\omega_j}\widehat{g}_k\right) \\ &\equiv \tau H_1(\tau) + H_2(\tau). \end{aligned} \tag{A4}$$

Here, we recognize H_1 and H_2 as DLR expansions themselves. Thus, H can be obtained at the DLR nodes τ_k by computing the DLR coefficients of H_1 and H_2 directly from those of F and G, at an $\mathcal{O}(r^2)$ cost, and then evaluating their DLR expansions to obtain the values $H(\tau_k) = \tau_k H_1(\tau_k) + H_2(\tau_k)$. We note that if one wishes to obtain the DLR coefficients of H directly, then it is slightly more efficient to precompute the matrix of multiplication by τ in its DLR coefficient representation and apply this directly to the computed vector of DLR coefficients of H_1. Adding the result to the vector of DLR coefficients of H_2 yields that of H.

Since

$$\begin{aligned} &\int_\tau^\beta d\tau' F(\beta-\tau')G(\tau'-\tau) \\ &\quad = \int_0^{\beta-\tau} d\tau' F(\beta-\tau-\tau')G(\tau') = H(\beta-\tau) \end{aligned} \tag{A5}$$

for $H(\tau) \equiv \int_0^\tau d\tau' F(\tau-\tau')G(\tau')$, convolutions of this form appearing in the single-particle Green's function diagrams can be reduced to the form (A2). One can therefore compute $H(\tau)$ by the method described above and a reflection $H(\tau) \mapsto H(\beta-\tau)$, a linear map which can be represented in the DLR basis.

We lastly mention that Eq. (A1) is given by

$$\begin{aligned} H(\tau) = &\sum_{j=1}^{r} K(\tau,\omega_j)(\tau - K(1,\omega_j))\widehat{f}_j \widehat{g}_j + \sum_{j=1}^{r} K(\tau,\omega_j) \\ &\times \left(\left(\sum_{\substack{k=1\\k\neq j}}^{r} \frac{\widehat{f}_k}{\omega_k-\omega_j}\right)\widehat{g}_j + \widehat{f}_j \sum_{\substack{k=1\\k\neq j}}^{r} \frac{\widehat{g}_k}{\omega_k-\omega_j}\right). \end{aligned} \tag{A6}$$

APPENDIX B: DECOMPOSITION OF THIRD-ORDER PSEUDOPARTICLE SELF-ENERGY DIAGRAM

We illustrate the decomposition procedure described in Sec. IV A for a third-order self-energy diagram:

$$\begin{aligned} \Sigma(\tau) &= \int_0^\tau d\tau_4 \int_0^{\tau_4} d\tau_3 \int_0^{\tau_3} d\tau_2 \int_0^{\tau_2} d\tau_1 \Delta_3(\tau-\tau_1)\Delta_2(\tau_4-\tau_2)\Delta_1(\tau_3)\mathcal{G}_5(\tau-\tau_4)\mathcal{G}_4(\tau_4-\tau_3)\mathcal{G}_3(\tau_3-\tau_2)\mathcal{G}_2(\tau_2-\tau_1)\mathcal{G}_1(\tau_1) \\ &= \sum_{\omega_k,\omega_l\le 0} \frac{\hat{\Delta}_{3k}\hat{\Delta}_{2l}}{K_k^-(0)K_l^-(0)} K_k^+(\tau)\int_0^\tau d\tau_4 \mathcal{G}_5(\tau-\tau_4)K_l^+(\tau_4)\int_0^{\tau_4} d\tau_3 \mathcal{G}_4(\tau_4-\tau_3)\Delta_1(\tau_3) \\ &\quad \times \int_0^{\tau_3} d\tau_2 \mathcal{G}_3(\tau_3-\tau_2)K_l^-(\tau_2)\int_0^{\tau_2} d\tau_1 \mathcal{G}_2(\tau_2-\tau_1)(\mathcal{G}_1 K_k^-)(\tau_1) \\ &\quad + \sum_{\omega_k\le 0,\omega_l>0} \frac{\hat{\Delta}_{3k}\hat{\Delta}_{2l}}{K_k^-(0)K_l^+(0)} K_k^+(\tau)\int_0^\tau d\tau_4 \mathcal{G}_5(\tau-\tau_4)\int_0^{\tau_4} d\tau_3 (\mathcal{G}_4 K_l^+)(\tau_4-\tau_3)\Delta_1(\tau_3) \\ &\quad \times \int_0^{\tau_3} d\tau_2 (\mathcal{G}_3 K_l^+)(\tau_3-\tau_2)\int_0^{\tau_2} d\tau_1 \mathcal{G}_2(\tau_2-\tau_1)(\mathcal{G}_1 K_k^-)(\tau_1) \\ &\quad + \sum_{\omega_k>0,\omega_l\le 0} \frac{\hat{\Delta}_{3k}\hat{\Delta}_{2l}}{(K_k^+(0))^3 K_l^-(0)} \int_0^\tau d\tau_4 (\mathcal{G}_5 K_k^+)(\tau-\tau_4)K_l^+(\tau_4)\int_0^{\tau_4} d\tau_3 (\mathcal{G}_4 K_k^+)(\tau_4-\tau_3)\Delta_1(\tau_3) \\ &\quad \times \int_0^{\tau_3} d\tau_2 (\mathcal{G}_3 K_k^+)(\tau_3-\tau_2)K_l^-(\tau_2)\int_0^{\tau_2} d\tau_1 (\mathcal{G}_2 K_k^+)(\tau_2-\tau_1)\mathcal{G}_1(\tau_1) \\ &\quad + \sum_{\omega_k,\omega_l>0} \frac{\hat{\Delta}_{3k}\hat{\Delta}_{2l}}{(K_k^+(0))^3 K_l^+(0)} \int_0^\tau d\tau_4 (\mathcal{G}_5 K_k^+)(\tau-\tau_4)\int_0^{\tau_4} d\tau_3 (\mathcal{G}_4 K_k^+ K_l^+)(\tau_4-\tau_3)\Delta_1(\tau_3) \\ &\quad \times \int_0^{\tau_3} d\tau_2 (\mathcal{G}_3 K_k^+ K_l^+)(\tau_3-\tau_2)\int_0^{\tau_2} d\tau_1 (\mathcal{G}_2 K_k^+)(\tau_2-\tau_1)\mathcal{G}_1(\tau_1). \end{aligned} \tag{B1}$$

Here, we have introduced the notation $(\mathcal{G}_i K_k^{\pm} K_l^{\pm})(\tau) \equiv \mathcal{G}_i(\tau) K(\tau, \pm\omega_k) K(\tau, \pm\omega_l)$. To obtain this result diagrammatically using the procedure described in Sec. V, we proceed step by step. We first decompose $\Delta_3(\tau - \tau_1)$:

$$\Sigma(\tau) =$$

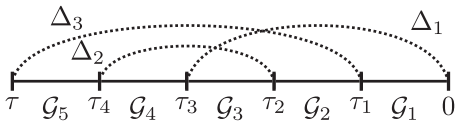

$$= \sum_{\omega_k \le 0} \frac{\widehat{\Delta}_{3k}}{K_k^-(0)}$$

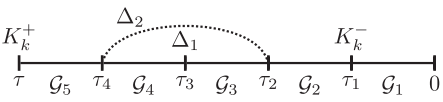

$$+ \sum_{\omega_k > 0} \frac{\widehat{\Delta}_{3k}}{(K_k^+(0))^3}$$

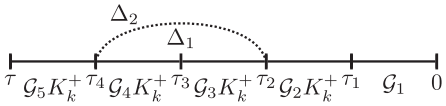

(B2)

Then, decomposing $\Delta_2(\tau_4 - \tau_2)$ in both of the resulting diagrams reproduces Eq. (B1):

$$\Sigma(\tau) = \sum_{\omega_k, \omega_l \le 0} \frac{\widehat{\Delta}_{3k}\widehat{\Delta}_{2l}}{K_k^-(0) K_l^-(0)}$$

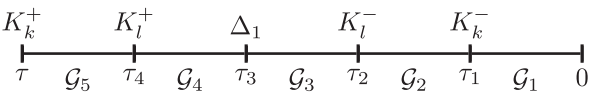

$$+ \sum_{\omega_k \le 0, \omega_l > 0} \frac{\widehat{\Delta}_{3k}\widehat{\Delta}_{2l}}{K_k^-(0) K_l^+(0)}$$

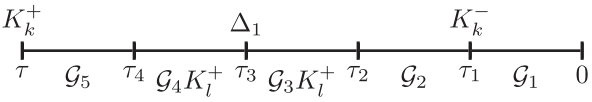

$$+ \sum_{\omega_k > 0, \omega_l \le 0} \frac{\widehat{\Delta}_{3k}\widehat{\Delta}_{2l}}{(K_k^+(0))^3 K_l^-(0)}$$

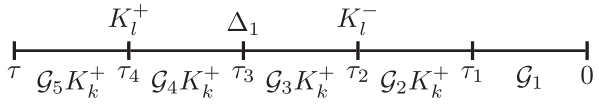

$$+ \sum_{\omega_k, \omega_l > 0} \frac{\widehat{\Delta}_{3k}\widehat{\Delta}_{2l}}{(K_k^+(0))^3 K_l^+(0)}$$

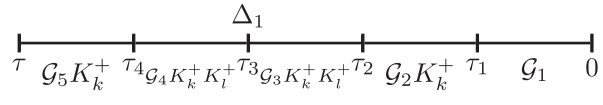

(B3)

APPENDIX C: WEAK COUPLING INTERACTION EXPANSION

In this appendix, we describe the application of our algorithm to the interaction expansion. We write the noninteracting part of the action using the quadratic term in Eq. (2) and the hybridization function in Eq. (3):

$$\mathcal{S}_0 = \sum_{\kappa,\lambda=1}^{n} \int_0^\beta d\tau c_\lambda^\dagger(\tau)[\partial_\tau - \epsilon_{\kappa\lambda} - \Delta_{\lambda\kappa}(\tau - \tau')] c_\kappa(\tau'). \quad \text{(C1)}$$

We then carry out an expansion in the interacting part of the action, given by

$$\mathcal{S}_{\text{int}} = \int_0^\beta d\tau H_{\text{int}} = \int_0^\beta d\tau \sum_{\kappa,\lambda,\mu,\nu=1}^{n} U_{\kappa\lambda\mu\nu} c_\kappa^\dagger(\tau) c_\lambda^\dagger(\tau) c_\nu(\tau) c_\mu(\tau), \quad \text{(C2)}$$

which yields an expression for the interacting propagator,

$$G_{\kappa\lambda}(\tau) = \frac{1}{Z} \sum_{m=0}^{\infty} \int_0^\beta d\tau_1 \cdots d\tau_m \times \langle \mathcal{T} H_{\text{int}}(\tau_1) \cdots H_{\text{int}}(\tau_m) c_\kappa^\dagger(\tau) c_\lambda(0) \rangle_{\mathcal{S}_0}, \quad \text{(C3)}$$

for $\lambda, \kappa = 1, \ldots, n$. Here, $\mathcal{T}$ is the time-ordering operator, and the expectation value is evaluated with respect to the noninteracting part of the action: $\langle \cdot \rangle_{\mathcal{S}_0} = \text{Tr}[e^{-\mathcal{S}_0} \cdot]$. By the linked cluster theorem, all disconnected diagrams in the expansion cancel with the partition function Z, and we need only consider connected diagrams. The expectation value in Eq. (C3) can be evaluated using Wick's theorem, and the noninteracting propagator is given by the Weiss Green's function $\mathcal{G}_0$, which satisfies the Dyson equation $\mathcal{G}_0 = g_0 + g_0 \circledast \Delta \circledast \mathcal{G}_0$. Here, the convolution is defined as

$$(a \circledast b)_{jk}(\tau) = \sum_{l=1}^{n} \int_0^\beta d\tau' a_{jl}(\tau - \tau') b_{lk}(\tau'),$$

and the noninteracting propagator is given by $g_0(\tau) = K(\tau, \epsilon - \mu)$, with ϵ the single-particle Hamiltonian

(quadratic part of H_{loc}), K defined by Eq. (20), and μ the chemical potential.

The propagator $G(\tau)$ is obtained by first evaluating the self-energy $\Sigma(\tau)$ and then solving the Dyson equation $G = \mathcal{G}_0 + \mathcal{G}_0 \circledast \Sigma \circledast G$. One can represent the self-energy either using a bare expansion, in which diagrams depend on the bare propagator $\mathcal{G}_0$, or a bold expansion, in which diagrams depend on the full propagator G. For concreteness, we focus on the case of the bare expansion, but the procedure described below is consistent with both schemes. We note, however, that the bold scheme requires solving the Dyson equation self-consistently.

The first-order terms of the bare expansion are given by the Hartree and Fock diagrams, which depend only on the single-particle density matrix. The first retarded diagrams appear at second order, with a representative example given by

$$\Sigma_{\alpha\beta}(\tau) = -U_{\beta'\gamma\beta\gamma'} U^{\alpha\delta\alpha'\delta'} \mathcal{G}_{0,\alpha'\beta'}(\tau) \mathcal{G}_{0,\gamma'\delta}(-\tau) \mathcal{G}_{0,\delta'\gamma}(\tau). \quad \text{(C4)}$$

Here, we use the Einstein notation that all repeated indices are summed over. In general, the second-order diagrams for the weak coupling expansion are similar to the NCA diagrams for the strong-coupling expansion, in that they involve only multiplications in imaginary-time.

The first diagrams involving imaginary-time integration appear at third order. A representative example is

$$\begin{aligned}\Sigma_{\alpha\beta}(\tau) = & -U_{\beta'\delta\beta\delta'} U_{\gamma\epsilon\gamma'\epsilon'} U_{\alpha\omega\alpha'\omega'} \mathcal{G}_{0,\delta'\omega}(-\tau) \\ & \times \int_0^\beta d\tau_1 \mathcal{G}_{0,\alpha'\gamma}(\tau - \tau_1) \mathcal{G}_{0,\omega'\epsilon}(\tau - \tau_1) \\ & \times \mathcal{G}_{0,\gamma'\beta'}(\tau_1) \mathcal{G}_{0,\epsilon'\delta}(\tau_1). \end{aligned} \quad \text{(C5)}$$

We see that the third-order weak coupling diagrams have a simple convolutional structure, precisely of the form (A1), and the DLR-based method described in Appendix A can be directly used to evaluate them. We refer the reader to Ref. [74] for the expressions for the other third-order diagrams, which have a similar structure.

Remark 4. We pause to consider the summation over orbital indices, which we have thus far assumed is carried out explicitly. For multiorbital systems, this leads to a large number of terms, growing exponentially with the diagram order. Methods based on sparsity or decomposability of tensors can, in some cases, be used to handle this issue, and one must verify their compatibility with our approach to imaginary-time integration. If the interaction tensor is sparse, the orbital index sums can be taken over a subset of terms, which is evidently compatible with our approach. This is the case in many physically interesting settings: For example, in cubic crystals in which d orbitals are split into e_g and t_{2g} manifolds, the Coulomb integral is given by the Slater-Kanamori interaction, and for the t_{2g} subspace, the interaction tensor has only 21 out of 81 nonzero entries [94,118]. More sophisticated schemes, such as Cholesky decomposition [119], density fitting [120,121], tensor hypercontraction [122,123], and the canonical polyadic decomposition [124–126], aim to decompose the interaction tensor using a low-rank structure, but these are typically applied in quantum chemistry or real materials calculations in which the orbital index dimension is significantly larger than that considered here. Although schemes of this type would likely also be compatible with our approach, further research is needed to determine which, if any, would be appropriate, and this question is outside the scope of the present work. Thus, in the remainder of this appendix, we consider explicit summation over orbital indices (or, in the sparse case, a subset of them) and, for simplicity, focus on each term separately. Reverting to the notation used in the description of our scheme for strong-coupling diagrams, we refer to different components of the bare electron propagator $\mathcal{G}_0$ as $\mathcal{G}_1$, $\mathcal{G}_2$, etc., in lieu of orbital indices, notating that, unlike in the strong-coupling case, each $\mathcal{G}_k$ is a scalar-valued function.

The first nonconvolutional diagrams appear at fourth order. In total, there are 12 topologically distinct fourth-order diagrams, shown in Fig. 5. As for the third-order diagrams, the diagrams in the first two rows can be written as nested sequences of products and convolutions [74] and evaluated using our efficient convolution scheme. For example, each orbital index combination of the first diagram in the first row of Fig. 5 takes the form

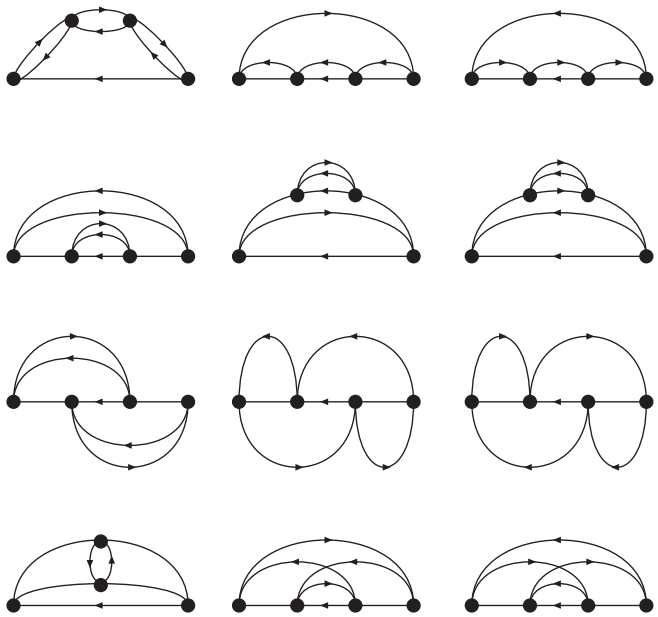

FIG. 5. Fourth-order self-energy diagrams for the weak coupling expansion of the Anderson impurity problem assuming a paramagnetic phase at half filling. Lines represent the electronic propagator $\mathcal{G}_0(G)$ for the bare (bold) expansion, and dots correspond to the interaction vertices U.

$$\Sigma(\tau) = \mathcal{G}_7(\tau) \int_0^\beta d\tau_2 \int_0^\beta d\tau_1 \mathcal{G}_6(\tau - \tau_1)\mathcal{G}_5(\tau - \tau_1) \times \mathcal{G}_4(\tau_1 - \tau_2)\mathcal{G}_3(\tau_1 - \tau_2)\mathcal{G}_2(\tau_2)\mathcal{G}_1(\tau_2). \tag{C6}$$

We note that the diagrams in the second row are not irreducible, and in the case of the bold expansion, they would be omitted.

On the other hand, the diagrams in the third and fourth rows of Fig. 5 cannot be expressed in terms of nested convolutions, and we must apply our decomposition scheme. For example, for the first diagram in the third row, we obtain expressions of the form

$$\Sigma(\tau) = \int_0^\beta d\tau_2 \int_0^\beta d\tau_1 \mathcal{G}_7(\tau - \tau_2) \times \mathcal{G}_6(\tau_2)\mathcal{G}_5(-\tau_2)\mathcal{G}_4(\tau_2 - \tau_1)\mathcal{G}_3(\tau_1) \times \mathcal{G}_2(\tau - \tau_1)\mathcal{G}_1(\tau_1 - \tau). \tag{C7}$$

Structurally, this diagram somewhat resembles the strong-coupling OCA diagrams, but here the integral is taken over the full square $[0, \beta]^2$ rather than a time-ordered subset. To avoid discontinuities, we divide the integral into six parts, each corresponding to an ordering of the variables τ, τ_1, and τ_2:

$$\int_0^\beta d\tau_2 \int_0^\beta d\tau_1 = \int_0^\tau d\tau_2 \int_0^{\tau_2} d\tau_1 + \int_0^\tau d\tau_1 \int_0^{\tau_1} d\tau_2 + \int_\tau^\beta d\tau_2 \int_0^\tau d\tau_1 + \int_\tau^\beta d\tau_1 \int_0^\tau d\tau_2 + \int_\tau^\beta d\tau_2 \int_{\tau_2}^\beta d\tau_1 + \int_\tau^\beta d\tau_1 \int_{\tau_1}^\beta d\tau_2.$$

The first two terms are structurally equivalent to the strong-coupling OCA self-energy diagrams, the third and fourth to the OCA single-particle Green's function diagrams, and, up to a simple change of variables, the fifth and sixth also to the OCA self-energy diagrams. We can therefore apply the same methodology with only minor modifications, in each case expanding a single function in the DLR basis in order to decompose the diagram. The computational complexity of each such diagram evaluation is therefore the same as for the strong-coupling OCA diagrams, with two important differences: (1) six terms must be computed instead of one, and (2) the functions $\mathcal{G}_k$ are $n \times n$ matrix valued, rather than $2^n \times 2^n$ matrix valued.

It is straightforward to verify that the other fourth-order diagrams in the third and fourth rows of Fig. 5 have a similar structure: Each has a backbone of propagators whose convolutional structure is broken by propagators coupling nonadjacent time variables. At fourth order, the convolutional structure can be reinstated by separating variables in at most two functions, as in the third-order strong-coupling diagrams. All higher-order self-energy diagrams share an analogous pattern, as in the strong-coupling case, though as the number of integration variables grows, the integrals must be split into a factorially growing number of time-ordered terms.

[1] A. Georges, G. Kotliar, W. Krauth, and M. J. Rozenberg, *Dynamical mean-field theory of strongly correlated fermion systems and the limit of infinite dimensions*, Rev. Mod. Phys. **68**, 13 (1996).

[2] E. Gull, A. J. Millis, A. I. Lichtenstein, A. N. Rubtsov, M. Troyer, and P. Werner, *Continuous-time Monte Carlo methods for quantum impurity models*, Rev. Mod. Phys. **83**, 349 (2011).

[3] K. Van Houcke, E. Kozik, N. Prokof'ev, and B. Svistunov, *Diagrammatic Monte Carlo*, Phys. Procedia **6**, 95 (2010).

[4] G. Onida, L. Reining, and A. Rubio, *Electronic excitations: Density-functional versus many-body Green's-function approaches*, Rev. Mod. Phys. **74**, 601 (2002).

[5] L. Hedin, *New method for calculating the one-particle Green's function with application to the electron-gas problem*, Phys. Rev. **139**, A796 (1965).

[6] D. Golze, M. Dvorak, and P. Rinke, *The GW compendium: A practical guide to theoretical photoemission spectroscopy*, Front. Chem. **7**, 377 (2019).

[7] J. Deslippe, G. Samsonidze, D. A. Strubbe, M. Jain, M. L. Cohen, and S. G. Louie, *BerkeleyGW: A massively parallel computer package for the calculation of the quasiparticle and optical properties of materials and nanostructures*, Comput. Phys. Commun. **183**, 1269 (2012).

[8] T. A. Costi, J. Kroha, and P. Wölfle, *Spectral properties of the Anderson impurity model: Comparison of numerical-renormalization-group and noncrossing-approximation results*, Phys. Rev. B **53**, 1850 (1996).

[9] J. Kroha and P. Wölfle, *Fermi and non-Fermi liquid behavior in quantum impurity systems: Conserving slave boson theory*, in *Advances in Solid State Physics 39*, edited by B. Kramer (Springer, Berlin, Heidelberg, 1999), pp. 271–280.

[10] H. Keiter and J. Kimball, *Diagrammatic approach to the Anderson model for dilute alloys*, J. Appl. Phys. **42**, 1460 (1971).

[11] N. Grewe and H. Keiter, *Diagrammatic approach to the intermediate-valence compounds*, Phys. Rev. B **24**, 4420 (1981).

[12] M. Eckstein and P. Werner, *Nonequilibrium dynamical mean-field calculations based on the noncrossing approximation and its generalizations*, Phys. Rev. B **82**, 115115 (2010).

[13] K. Haule, S. Kirchner, J. Kroha, and P. Wölfle, *Anderson impurity model at finite Coulomb interaction U: Generalized noncrossing approximation*, Phys. Rev. B **64**, 155111 (2001).

[14] T. Pruschke and N. Grewe, *The Anderson model with finite Coulomb repulsion*, Z. Phys. B **74**, 439 (1989).

[15] E. Gull, D. R. Reichman, and A. J. Millis, *Bold-line diagrammatic Monte Carlo method: General formulation and application to expansion around the noncrossing approximation*, Phys. Rev. B **82**, 075109 (2010).

[16] K. Haule, *Strong coupling quantum impurity solver on the real and imaginary axis*, arXiv:2311.09412.

[17] K. Haule and G. Kotliar, *Strongly correlated superconductivity: A plaquette dynamical mean-field theory study*, Phys. Rev. B **76**, 104509 (2007).

[18] D. Golež, M. Eckstein, and P. Werner, *Dynamics of screening in photodoped Mott insulators*, Phys. Rev. B **92**, 195123 (2015).

[19] N. Bittner, D. Golež, H. U. R. Strand, M. Eckstein, and P. Werner, *Coupled charge and spin dynamics in a photoexcited doped Mott insulator*, Phys. Rev. B **97**, 235125 (2018).

[20] B. M. de Souza Melo, L. G. D. da Silva, A. R. Rocha, and C. Lewenkopf, *Quantitative comparison of Anderson impurity solvers applied to transport in quantum dots*, J. Phys. Condens. Matter **32**, 095602 (2019).

[21] V. Vildosola, L. Pourovskii, L. O. Manuel, and P. Roura-Bas, *Reliability of the one-crossing approximation in describing the Mott transition*, J. Phys. Condens. Matter **27**, 485602 (2015).

[22] R. Korytár and N. Lorente, *Multi-orbital non-crossing approximation from maximally localized Wannier functions: The Kondo signature of copper phthalocyanine on Ag(100)*, J. Phys. Condens. Matter **23**, 355009 (2011).

[23] H. U. R. Strand, D. Golež, M. Eckstein, and P. Werner, *Hund's coupling driven photocarrier relaxation in the two-band Mott insulator*, Phys. Rev. B **96**, 165104 (2017).

[24] D. Golež, M. Eckstein, and P. Werner, *Multiband nonequilibrium $GW+\mathrm{EDMFT}$ formalism for correlated insulators*, Phys. Rev. B **100**, 235117 (2019).

[25] K. Haule, C.-H. Yee, and K. Kim, *Dynamical mean-field theory within the full-potential methods: Electronic structure of* $\mathrm{CeIrIn_5}$, $\mathrm{CeCoIn_5}$, *and* $\mathrm{CeRhIn_5}$, Phys. Rev. B **81**, 195107 (2010).

[26] A. J. Kim, J. Li, M. Eckstein, and P. Werner, *Pseudoparticle vertex solver for quantum impurity models*, Phys. Rev. B **106**, 085124 (2022).

[27] A. J. Kim, K. Lenk, J. Li, P. Werner, and M. Eckstein, *Vertex-based diagrammatic treatment of light-matter-coupled systems*, Phys. Rev. Lett. **130**, 036901 (2023).

[28] A. N. Rubtsov, V. V. Savkin, and A. I. Lichtenstein, *Continuous-time quantum Monte Carlo method for fermions*, Phys. Rev. B **72**, 035122 (2005).

[29] P. Werner, A. Comanac, L. de' Medici, M. Troyer, and A. J. Millis, *Continuous-time solver for quantum impurity models*, Phys. Rev. Lett. **97**, 076405 (2006).

[30] P. Werner and A. J. Millis, *Hybridization expansion impurity solver: General formulation and application to Kondo lattice and two-orbital models*, Phys. Rev. B **74**, 155107 (2006).

[31] K. Haule, *Quantum Monte Carlo impurity solver for cluster dynamical mean-field theory and electronic structure calculations with adjustable cluster base*, Phys. Rev. B **75**, 155113 (2007).

[32] G. Kotliar, S. Y. Savrasov, K. Haule, V. S. Oudovenko, O. Parcollet, and C. A. Marianetti, *Electronic structure calculations with dynamical mean-field theory*, Rev. Mod. Phys. **78**, 865 (2006).

[33] N. Prokof'ev and B. Svistunov, *Bold diagrammatic Monte Carlo technique: When the sign problem is welcome*, Phys. Rev. Lett. **99**, 250201 (2007).

[34] T. Hahn, S. Klimin, J. Tempere, J. T. Devreese, and C. Franchini, *Diagrammatic Monte Carlo study of Fröhlich polaron dispersion in two and three dimensions*, Phys. Rev. B **97**, 134305 (2018).

[35] A. S. Mishchenko, N. V. Prokof'ev, A. Sakamoto, and B. V. Svistunov, *Diagrammatic quantum Monte Carlo study of the Fröhlich polaron*, Phys. Rev. B **62**, 6317 (2000).

[36] R. Rossi, *Determinant diagrammatic Monte Carlo algorithm in the thermodynamic limit*, Phys. Rev. Lett. **119**, 045701 (2017).

[37] F. Šimkovic and E. Kozik, *Determinant Monte Carlo for irreducible Feynman diagrams in the strongly correlated regime*, Phys. Rev. B **100**, 121102(R) (2019).

[38] A. Moutenet, W. Wu, and M. Ferrero, *Determinant Monte Carlo algorithms for dynamical quantities in fermionic systems*, Phys. Rev. B **97**, 085117 (2018).

[39] T. Schäfer *et al.*, *Tracking the footprints of spin fluctuations: A multimethod, multimessenger study of the two-dimensional Hubbard model*, Phys. Rev. X **11**, 011058 (2021).

[40] M. Maček, P. T. Dumitrescu, C. Bertrand, B. Triggs, O. Parcollet, and X. Waintal, *Quantum quasi-Monte Carlo technique for many-body perturbative expansions*, Phys. Rev. Lett. **125**, 047702 (2020).

[41] H. U. R. Strand, J. Kleinhenz, and I. Krivenko, *Inchworm quasi Monte Carlo for quantum impurities*, arXiv:2310.16957.

[42] E. Eidelstein, E. Gull, and G. Cohen, *Multiorbital quantum impurity solver for general interactions and hybridizations*, Phys. Rev. Lett. **124**, 206405 (2020).

[43] G. Zhang and E. Pavarini, *Mott transition, spin-orbit effects, and magnetism in* $\mathrm{Ca_2RuO_4}$, Phys. Rev. B **95**, 075145 (2017).

[44] G. Zhang, E. Gorelov, E. Sarvestani, and E. Pavarini, *Fermi surface of* $\mathrm{Sr_2RuO_4}$*: Spin-orbit and anisotropic Coulomb interaction effects*, Phys. Rev. Lett. **116**, 106402 (2016).

[45] G. Cohen, E. Gull, D. R. Reichman, and A. J. Millis, *Taming the dynamical sign problem in real-time evolution of quantum many-body problems*, Phys. Rev. Lett. **115**, 266802 (2015).

[46] Y. Núñez Fernández, M. Jeannin, P. T. Dumitrescu, T. Kloss, J. Kaye, O. Parcollet, and X. Waintal, *Learning Feynman diagrams with tensor trains*, Phys. Rev. X **12**, 041018 (2022).

[47] A. Erpenbeck, W.-T. Lin, T. Blommel, L. Zhang, S. Iskakov, L. Bernheimer, Y. Núñez Fernández, G. Cohen, O. Parcollet, X. Waintal, and E. Gull, *Tensor train continuous time solver for quantum impurity models*, Phys. Rev. B **107**, 245135 (2023).

[48] J. Kaye, K. Chen, and O. Parcollet, *Discrete Lehmann representation of imaginary time Green's functions*, Phys. Rev. B **105**, 235115 (2022).

[49] D. Sutter *et al.*, *Hallmarks of Hunds coupling in the Mott insulator* $\mathrm{Ca_2RuO_4}$, Nat. Commun. **8**, 15176 (2017).

[50] Q. Han and A. Millis, *Lattice energetics and correlation-driven metal-insulator transitions: The case of* Ca_2RuO_4, Phys. Rev. Lett. **121**, 067601 (2018).
[51] A. Liebsch and H. Ishida, *Subband filling and Mott transition in* $Ca_{2-x}Sr_xRuO_4$, Phys. Rev. Lett. **98**, 216403 (2007).
[52] A. B. Georgescu and A. J. Millis, *Quantifying the role of the lattice in metal–insulator phase transitions*, Commun. Phys. **5**, 135 (2022).
[53] H. Hao, A. Georges, A. J. Millis, B. Rubenstein, Q. Han, and H. Shi, *Metal-insulator and magnetic phase diagram of* Ca_2RuO_4 *from auxiliary field quantum Monte Carlo and dynamical mean field theory*, Phys. Rev. B **101**, 235110 (2020).
[54] F. Aryasetiawan and S. Biermann, *Generalized Hedin's equations for quantum many-body systems with spin-dependent interactions*, Phys. Rev. Lett. **100**, 116402 (2008).
[55] M. Jarrell, *Hubbard model in infinite dimensions: A quantum Monte Carlo study*, Phys. Rev. Lett. **69**, 168 (1992).
[56] G. Beylkin and L. Monzón, *On approximation of functions by exponential sums*, Appl. Comput. Harmon. Anal. **19**, 17 (2005).
[57] G. Beylkin and L. Monzón, *Approximation by exponential sums revisited*, Appl. Comput. Harmon. Anal. **28**, 131 (2010).
[58] Y. Zhang, C. Zhuang, and S. Jiang, *Fast one-dimensional convolution with general kernels using sum-of-exponential approximation*, Commun. Comput. Phys. **29**, 1570 (2021).
[59] Z. Gao, J. Liang, and Z. Xu, *A kernel-independent sum-of-exponentials method*, J. Sci. Comput. **93**, 40 (2022).
[60] L. Greengard and P. Lin, *Spectral approximation of the free-space heat kernel*, Appl. Comput. Harmon. Anal. **9**, 83 (2000).
[61] S. Jiang, L. Greengard, and S. Wang, *Efficient sum-of-exponentials approximations for the heat kernel and their applications*, Adv. Comput. Math. **41**, 529 (2015).
[62] J. G. Hoskins, J. Kaye, M. Rachh, and J. C. Schotland, *A fast, high-order numerical method for the simulation of single-excitation states in quantum optics*, J. Comput. Phys. **473**, 111723 (2023).
[63] B. Alpert, L. Greengard, and T. Hagstrom, *Nonreflecting boundary conditions for the time-dependent wave equation*, J. Comput. Phys. **180**, 270 (2002).
[64] S. Jiang and L. Greengard, *Fast evaluation of nonreflecting boundary conditions for the Schrödinger equation in one dimension*, Comput. Math. Appl. **47**, 955 (2004).
[65] S. Jiang and L. Greengard, *Efficient representation of nonreflecting boundary conditions for the time-dependent Schrödinger equation in two dimensions*, Commun. Pure Appl. Math. **61**, 261 (2008).
[66] L. Greengard and V. Rokhlin, *A new version of the fast multipole method for the Laplace equation in three dimensions*, Acta Numer. **6**, 229 (1997).
[67] H. Cheng, L. Greengard, and V. Rokhlin, *A fast adaptive multipole algorithm in three dimensions*, J. Comput. Phys. **155**, 468 (1999).
[68] T. Hrycak and V. Rokhlin, *An improved fast multipole algorithm for potential fields*, SIAM J. Sci. Comput. **19**, 1804 (1998).
[69] S. Jiang and L. Greengard, *Approximating the Gaussian as a sum of exponentials and its applications to the fast Gauss transform*, Commun. Comput. Phys. **31**, 1 (2021).
[70] R. Pei, T. Askham, L. Greengard, and S. Jiang, *A fast method for imposing periodic boundary conditions on arbitrarily-shaped lattices in two dimensions*, J. Comput. Phys. **474**, 111792 (2023).
[71] Z. Gimbutas, N. F. Marshall, and V. Rokhlin, *A fast simple algorithm for computing the potential of charges on a line*, Appl. Comput. Harmon. Anal. **49**, 815 (2020).
[72] A. Barnett, P. Greengard, and M. Rachh, *Uniform approximation of common Gaussian process kernels using equispaced Fourier grids*, Appl. Comput. Harmon. Anal. **71**, 101640 (2024).
[73] E. Gull, P. Werner, A. Millis, and M. Troyer, *Performance analysis of continuous-time solvers for quantum impurity models*, Phys. Rev. B **76**, 235123 (2007).
[74] N. Tsuji and P. Werner, *Nonequilibrium dynamical mean-field theory based on weak-coupling perturbation expansions: Application to dynamical symmetry breaking in the Hubbard model*, Phys. Rev. B **88**, 165115 (2013).
[75] C. Bertrand, S. Florens, O. Parcollet, and X. Waintal, *Reconstructing nonequilibrium regimes of quantum many-body systems from the analytical structure of perturbative expansions*, Phys. Rev. X **9**, 041008 (2019).
[76] M. Schüler, D. Golež, Y. Murakami, N. Bittner, A. Herrmann, H. U. Strand, P. Werner, and M. Eckstein, *NESSi: The non-equilibrium systems simulation package*, Comput. Phys. Commun. **257**, 107484 (2020).
[77] B. Fornberg and J. A. Reeger, *An improved Gregory-like method for 1-D quadrature*, Numer. Math. **141**, 1 (2019).
[78] B. Fornberg, *Improving the accuracy of the trapezoidal rule*, SIAM Rev. **63**, 167 (2021).
[79] B. K. Alpert, *Hybrid Gauss-trapezoidal quadrature rules*, SIAM J. Sci. Comput. **20**, 1551 (1999).
[80] J. Kaye, K. Chen, and H. U. R. Strand, *libdlr: Efficient imaginary time calculations using the discrete Lehmann representation*, Comput. Phys. Commun. **280**, 108458 (2022).
[81] H. Shinaoka, J. Otsuki, M. Ohzeki, and K. Yoshimi, *Compressing Green's function using intermediate representation between imaginary-time and real-frequency domains*, Phys. Rev. B **96**, 035147 (2017).
[82] N. Chikano, J. Otsuki, and H. Shinaoka, *Performance analysis of a physically constructed orthogonal representation of imaginary-time Green's function*, Phys. Rev. B **98**, 035104 (2018).
[83] J. Li, M. Wallerberger, N. Chikano, C.-N. Yeh, E. Gull, and H. Shinaoka, *Sparse sampling approach to efficient ab initio calculations at finite temperature*, Phys. Rev. B **101**, 035144 (2020).
[84] N. Sheng, A. Hampel, S. Beck, O. Parcollet, N. Wentzell, J. Kaye, and K. Chen, *Low-rank Green's function representations applied to dynamical mean-field theory*, Phys. Rev. B **107**, 245123 (2023).
[85] H. LaBollita, J. Kaye, and A. Hampel, *Stabilizing the calculation of the self-energy in dynamical mean-field theory using constrained residual minimization*, arXiv:2310.01266.

[86] J. Kaye and H. U. R. Strand, *A fast time domain solver for the equilibrium Dyson equation*, Adv. Comput. Math. **49**, 63, (2023).

[87] C.-N. Yeh, S. Iskakov, D. Zgid, and E. Gull, *Fully self-consistent finite-temperature GW in Gaussian Bloch orbitals for solids*, Phys. Rev. B **106**, 235104 (2022).

[88] X. Cai, T. Wang, N. V. Prokof'ev, B. V. Svistunov, and K. Chen, *Superconductivity in the uniform electron gas: Irrelevance of the Kohn-Luttinger mechanism*, Phys. Rev. B **106**, L220502 (2022).

[89] H. Shinaoka, N. Chikano, E. Gull, J. Li, T. Nomoto, J. Otsuki, M. Wallerberger, T. Wang, and K. Yoshimi, *Efficient ab initio many-body calculations based on sparse modeling of Matsubara Green's function*, SciPost Phys. Lect. Notes 63 (2022).

[90] C. Mejuto-Zaera, L. Zepeda-Núñez, M. Lindsey, N. Tubman, B. Whaley, and L. Lin, *Efficient hybridization fitting for dynamical mean-field theory via semi-definite relaxation*, Phys. Rev. B **101**, 035143 (2020).

[91] H. Shinaoka and Y. Nagai, *Sparse modeling of large-scale quantum impurity models with low symmetries*, Phys. Rev. B **103**, 045120 (2021).

[92] Z. Huang, E. Gull, and L. Lin, *Robust analytic continuation of Green's functions via projection, pole estimation, and semidefinite relaxation*, Phys. Rev. B **107**, 075151 (2023).

[93] J. Kaye and H. U. R. Strand, libdlr v1.0.0 (2022).

[94] J. Kanamori, *Electron correlation and ferromagnetism of transition metals*, Prog. Theor. Phys. **30**, 275 (1963).

[95] S. Hoshino and P. Werner, *Electronic orders in multi-orbital Hubbard models with lifted orbital degeneracy*, Phys. Rev. B **93**, 155161 (2016).

[96] P. Werner, E. Gull, M. Troyer, and A. J. Millis, *Spin freezing transition and non-Fermi-liquid self-energy in a three-orbital model*, Phys. Rev. Lett. **101**, 166405 (2008).

[97] A. E. Antipov, Q. Dong, J. Kleinhenz, G. Cohen, and E. Gull, *Currents and Green's functions of impurities out of equilibrium: Results from inchworm quantum Monte Carlo*, Phys. Rev. B **95**, 085144 (2017).

[98] O. Parcollet, M. Ferrero, T. Ayral, H. Hafermann, I. Krivenko, L. Messio, and P. Seth, *TRIQS: A toolbox for research on interacting quantum systems*, Comput. Phys. Commun. **196**, 398 (2015).

[99] P. Seth, I. Krivenko, M. Ferrero, and O. Parcollet, *TRIQS/CTHYB: A continuous-time quantum Monte Carlo hybridisation expansion solver for quantum impurity problems*, Comput. Phys. Commun. **200**, 274 (2016).

[100] H. Hafermann, K. R. Patton, and P. Werner, *Improved estimators for the self-energy and vertex function in hybridization-expansion continuous-time quantum Monte Carlo simulations*, Phys. Rev. B **85**, 205106 (2012).

[101] P. Gunacker, M. Wallerberger, T. Ribic, A. Hausoel, G. Sangiovanni, and K. Held, *Worm-improved estimators in continuous-time quantum Monte Carlo*, Phys. Rev. B **94**, 125153 (2016).

[102] J. Kaufmann, P. Gunacker, A. Kowalski, G. Sangiovanni, and K. Held, *Symmetric improved estimators for continuous-time quantum Monte Carlo*, Phys. Rev. B **100**, 075119 (2019).

[103] P. Gunacker, M. Wallerberger, E. Gull, A. Hausoel, G. Sangiovanni, and K. Held, *Continuous-time quantum Monte Carlo using worm sampling*, Phys. Rev. B **92**, 155102 (2015).

[104] M. Wallerberger, A. Hausoel, P. Gunacker, A. Kowalski, N. Parragh, F. Goth, K. Held, and G. Sangiovanni, *w2dynamics: Local one- and two-particle quantities from dynamical mean field theory*, Comput. Phys. Commun. **235**, 388 (2019).

[105] E. Gorelov, M. Karolak, T. O. Wehling, F. Lechermann, A. I. Lichtenstein, and E. Pavarini, *Nature of the Mott transition in* Ca_2RuO_4, Phys. Rev. Lett. **104**, 226401 (2010).

[106] S. Sugano, *Multiplets of Transition-Metal Ions in Crystals* (Elsevier, New York, 2012).

[107] G. Khaliullin, *Excitonic magnetism in van Vleck–type* d^4 *Mott insulators*, Phys. Rev. Lett. **111**, 197201 (2013).

[108] A. Akbari and G. Khaliullin, *Magnetic excitations in a spin-orbit-coupled* d^4 *Mott insulator on the square lattice*, Phys. Rev. B **90**, 035137 (2014).

[109] J. Mravlje, M. Aichhorn, T. Miyake, K. Haule, G. Kotliar, and A. Georges, *Coherence-incoherence crossover and the mass-renormalization puzzles in* Sr_2RuO_4, Phys. Rev. Lett. **106**, 096401 (2011).

[110] M. Braden, G. André, S. Nakatsuji, and Y. Maeno, *Crystal and magnetic structure of* Ca_2RuO_4*: Magnetoelastic coupling and the metal-insulator transition*, Phys. Rev. B **58**, 847 (1998).

[111] G. L. Stamokostas and G. A. Fiete, *Mixing of* $t_{2g} - e_g$ *orbitals in* 4*d and* 5*d transition metal oxides*, Phys. Rev. B **97**, 085150 (2018).

[112] G. Jackeli and G. Khaliullin, *Mott insulators in the strong spin-orbit coupling limit: From Heisenberg to a quantum compass and Kitaev models*, Phys. Rev. Lett. **102**, 017205 (2009).

[113] B. Kim, H. Ohsumi, T. Komesu, S. Sakai, T. Morita, H. Takagi, and T.-h. Arima, *Phase-sensitive observation of a spin-orbital Mott state in* Sr_2IrO_4, Science **323**, 1329 (2009).

[114] B. Lenz, C. Martins, and S. Biermann, *Spectral functions of* Sr_2IrO_4*: Theory versus experiment*, J. Phys. Condens. Matter **31**, 293001 (2019).

[115] B. H. Kim, G. Khaliullin, and B. I. Min, *Magnetic couplings, optical spectra, and spin-orbit exciton in* 5*d electron Mott insulator* Sr_2IrO_4, Phys. Rev. Lett. **109**, 167205 (2012).

[116] S. Grytsiuk, M. I. Katsnelson, E. G. C. P. van Loon, and M. Rösner, Nb_3Cl_8*: A prototypical layered Mott-Hubbard insulator*, npj Quantum Mater. **9**, 8 (2024).

[117] M. Aichhorn, L. Pourovskii, P. Seth, V. Vildosola, M. Zingl, O. E. Peil, X. Deng, J. Mravlje, G. J. Kraberger, C. Martins, M. Ferrero, and O. Parcollet, *TRIQS/DFTTools: A TRIQS application for ab initio calculations of correlated materials*, Comput. Phys. Commun. **204**, 200 (2016).

[118] F. Nilsson, L. Boehnke, P. Werner, and F. Aryasetiawan, *Multitier self-consistent* GW + EDMFT, Phys. Rev. Mater. **1**, 043803 (2017).

[119] N. H. F. Beebe and J. Linderberg, *Simplifications in the generation and transformation of two-electron integrals in*

molecular calculations, Int. J. Quantum Chem. **12**, 683 (1977).

[120] F. Weigend, M. Kattannek, and R. Ahlrichs, *Approximated electron repulsion integrals: Cholesky decomposition versus resolution of the identity methods*, J. Chem. Phys. **130**, 164106 (2009).

[121] X. Ren, P. Rinke, V. Blum, J. Wieferink, A. Tkatchenko, A. Sanfilippo, K. Reuter, and M. Scheffler, *Resolution-of-identity approach to Hartree–Fock, hybrid density functionals, RPA, MP2 and GW with numeric atom-centered orbital basis functions*, New J. Phys. **14**, 053020 (2012).

[122] J. Lu and L. Ying, *Compression of the electron repulsion integral tensor in tensor hypercontraction format with cubic scaling cost*, J. Comput. Phys. **302**, 329 (2015).

[123] C.-N. Yeh and M. A. Morales, *Low-scaling algorithm for the random phase approximation using tensor hypercontraction with k-point sampling*, J. Chem. Theory Comput. **19**, 6197 (2023).

[124] U. Benedikt, A. A. Auer, M. Espig, and W. Hackbusch, *Tensor decomposition in post-Hartree–Fock methods. I. Two-electron integrals and MP2*, J. Chem. Phys. **134**, 054118 (2011).

[125] K. Pierce, V. Rishi, and E. F. Valeev, *Robust approximation of tensor networks: Application to grid-free tensor factorization of the Coulomb interaction*, J. Chem. Theory Comput. **17**, 2217 (2021).

[126] K. Pierce and E. F. Valeev, *Efficient construction of canonical polyadic approximations of tensor networks*, J. Chem. Theory Comput. **19**, 71 (2023).

Correction: Sign errors below the summation in the second line of Eq. (37), in an inline equation in the text below Eq. (37), and below the summation in the third line of Eq. (38) have been fixed.